OXFORD

Journal of Petrology, 2023, **64**, 1–22
https://doi.org/10.1093/petrology/egad075
Advance access publication date 9 October 2023
Original Manuscript

Himalayan-like Crustal Melting and Differentiation in the Southern North American Cordilleran Anatectic Belt during the Laramide Orogeny: Coyote Mountains, Arizona

James B. Chapman [1,*], Cody Pridmore[2], Kevin Chamberlain[2], Gordon Haxel[3] and Mihai Ducea[4,5]

[1]Department of Earth, Environmental and Resource Sciences, University of Texas at El Paso, 500 W. University Ave., El Paso, TX 79968, USA
[2]Department of Geology and Geophysics, University of Wyoming, 1000 E. University Ave., Laramie, WY 82071, USA
[3]School of Earth Sciences and Environmental Sustainability, Northern Arizona University, 624 Knoles Dr., Flagstaff, AZ 86011, USA
[4]Department of Geosciences, University of Arizona, 1040 E. 4th St., Tucson, AZ 85721, USA
[5]Faculty of Geology and Geophysics, University of Bucharest, 6 Traian Vuia St., sector 2, Bucharest 020956, Romania

*Corresponding author. Telephone: +1 915 747 7556. Fax: +1 915 747 5073. E-mail: jbchapmanv@utep.edu

Abstract

The southern US and northern Mexican Cordillera experienced crustal melting during the Laramide orogeny (c. 80–40 Ma). The metamorphic sources of melt are not exposed at the surface; however, anatectic granites are present throughout the region, providing an opportunity to investigate the metamorphic processes associated with this orogeny. A detailed geochemical and petrochronological analysis of the Pan Tak Granite from the Coyote Mountains core complex in southern Arizona suggests that prograde metamorphism, melting, and melt crystallization occurred here from 62 to 42 Ma. Ti-in-zircon temperatures ($T_{Ti\text{-}zr}$) correlate with changes in zircon rare earth elements (REE) concentrations, and indicate prograde heating, mineral breakdown, and melt generation took place from 62 to 53 Ma. $T_{Ti\text{-}zr}$ increases from ~650 to 850 °C during this interval. A prominent gap in zircon ages is observed from 53 to 51 Ma and is interpreted to reflect the timing of peak metamorphism and melting, which caused zircon dissolution. The age gap is an inflection point in several geochemical-temporal trends that suggest crystallization and cooling dominated afterward, from 51 to 42 Ma. Supporting this interpretation is an increase in zircon U/Th and Hf, a decrease in $T_{Ti\text{-}zr}$, increasing zircon $(Dy/Yb)_n$, and textural evidence for coupled dissolution–reprecipitation processes that resulted in zircon (re)crystallization. In addition, whole rock REE, large ion lithophile elements, and major elements suggest that the Pan Tak Granite experienced advanced fractional crystallization during this time. High-silica, muscovite± garnet leucogranite dikes that crosscut two-mica granite represent more evolved residual melt compositions. The Pan Tak Granite was formed by fluid-deficient melting and biotite dehydration melting of meta-igneous protoliths, including Jurassic arc rocks and the Proterozoic Oracle Granite. The most likely causes of melting are interpreted to be a combination of (1) radiogenic heating and relaxation of isotherms associated with crustal thickening under a plateau environment, (2) heat and fluid transfer related to the Laramide continental arc, and (3) shear and viscous heating related to the deformation of the deep lithosphere. The characteristics and petrologic processes that created the Pan Tak Granite are strikingly similar to intrusive suites in the Himalayan leucogranite belt and further support the association between the North American Cordilleran anatectic belt and a major orogenic and thermal event during the Laramide orogeny.

Key words: anatexis; Cordilleran; crustal melting; Himalaya; Laramide; leucogranite; petrochronology; zircon

INTRODUCTION

The Himalayan leucogranite belt is an Oligocene to Miocene, ~3000 km long, intrusive province in southern Tibet that includes the High Himalayan leucogranite belt and the North Himalayan leucogranite belt (Guo & Wilson, 2012; Weinberg, 2016). It is the most famous and well-studied anatectic province on Earth and is central to understanding the tectonic evolution of the Himalayan-Tibetan orogen (Le Fort *et al.*, 1987; England *et al.*, 1992; Harris & Massey, 1994; Hodges, 1998; King *et al.*, 2011). One of the most striking features of the Himalayan leucogranite belt is that crustal melting, and the generation of anatectic granites has been a prolonged process. Most of the Himalayan leucogranites crystallized between 30 and 10 Ma and contain a relatively broad range of ages (commonly ~10 Myr) of U–Th–Pb accessory mineral ages (Zhang *et al.*, 2004; Lederer *et al.*, 2013; Rubatto *et al.*, 2013; Finch *et al.*, 2014; Kohn, 2014; Horton *et al.*, 2015; Cottle *et al.*, 2018; Ji *et al.*, 2020; Ding *et al.*, 2021). This phenomenon is observed from the regional scale to within a single rock sample and is generally interpreted to reflect the duration of partial melting, protracted crystallization, mineral resorption and regrowth, melt and fluid (re)mobilization, and the recycling of accessory minerals (Weinberg, 2016). Furthermore, an increasing number of studies have recognized that during this prolonged process, melts can undergo advanced fractionation to produce high-silica, strongly peraluminous leucogranite (Scaillet *et al.*, 1990, 1995; Liu *et al.*, 2014, 2019; Huang *et al.*, 2017; Yang *et al.*, 2019; Wang *et al.*, 2020; Wu *et al.*, 2020; Chen *et al.*, 2021). Regardless of the exact mechanisms involved, the picture that emerges is the existence of a hot, migmatitic, deep crust that remains close to the solidus

Received: January 11, 2023. **Revised:** September 27, 2023. **Accepted:** October 5, 2023

for up to tens of millions of years during orogenesis and can produce anatectic melts, which experience complex fluid–melt–rock interactions and are periodically extracted to be emplaced into the middle to upper crust. Geophysical studies suggest that melt is currently present beneath the Himalaya and Tibetan Plateau, which indicates that the deep crust may still be producing anatectic granites today (Nelson *et al.*, 1996; Unsworth *et al.*, 2005; Klemperer, 2006).

An orogenic plateau, similar to the Tibetan Plateau, called the Arizonaplano, has been postulated in the southern US and northern Mexican Cordillera during the Laramide orogeny (c. 80–40 Ma) (Chapman *et al.*, 2020; Jepson *et al.*, 2022). This region also experienced crustal melting during the Laramide orogeny and is part of the broader North American Cordilleran Anatectic Belt (Chapman *et al.*, 2021). However, there are no known exposures of migmatite related to the Laramide orogeny in the southern US and northern Mexican Cordillera, hampering investigations into the thermal and metamorphic history of the region. Anatectic granitic rocks, chiefly emplaced into the middle crust and exposed in the exhumed footwalls of metamorphic core complexes (e.g. Fornash *et al.*, 2013; Ducea *et al.*, 2020; Scoggin *et al.*, 2021), are one of the few sources of data for understanding metamorphism and deep crustal melting processes during the Laramide orogeny in this region.

The North American Cordilleran Anatectic Belt is the world's best example of an anatectic belt in a Cordilleran orogenic system and provides an analog for processes inferred to occur at depth in modern orogens like the Andes. For example, the Altiplano-Puna magma body is a zone of partial melting at ~20 km depth (Delph *et al.*, 2017; Ward *et al.*, 2017) that may be equivalent to the anatectic granites exposed in the North American Cordilleran Anatectic Belt. Associated with the Altiplano-Puna magma body is the 10 Ma to present Altiplano-Puna volcanic complex that is considered a product of 'eruptive migmatites' (Schilling *et al.*, 2006). Heat and mass input from the mantle contributed to the formation of the Altiplano-Puna volcanic complex, but it is fundamentally the product of crustal melting in an orogenic plateau characterized by high heat flow and no erosion (Ducea *et al.*, 2013).

Here, we report an intrusive suite from the anatectic belt in southern Arizona—the Pan Tak Granite in the Coyote Mountains (Wright & Haxel, 1982) (Figs 1 and 2). We present new age, geochemical, radiogenic isotope (Hf, Nd, Sr) and O isotope data from the Pan Tak Granite, including a detailed zircon petrochronological analysis. The intrusive history, differentiation trends, geochemistry, and crystallization sequence of the Pan Tak Granite are remarkably similar to many intrusive suites in the Himalayan leucogranite belt and can be interpreted in terms of metamorphic and anatectic processes. A critical observation is that the zircon cargo of the Pan Tak Granite includes antecrysts that formed in the deep crust, presumably in a migmatitic source, and retain information on the earliest history of partial melting. These data from the Pan Tak Granite provide the first constraints on the timing and timescales of metamorphism, peak metamorphic conditions, and mechanisms of crustal melting for this region.

GEOLOGIC BACKGROUND

The Coyote Mountains form the footwall of the Coyote Mountains metamorphic core complex that experienced rapid exhumation from 29 to 24 Ma (Gottardi *et al.*, 2020). The core complex is one of several found in southern Arizona, USA, and northern Sonora, Mexico, that contains Paleocene to Eocene age anatectic granites (Chapman *et al.*, 2021). Other examples include the Wilderness Suite in the Catalina-Rincon Mountains (Fornash *et al.*, 2013; Ducea *et al.*, 2020), the Relleno Suite in the Piñaleno Mountains (Scoggin *et al.*, 2021), and the Presumido Peak Granite in the Pozo Verde Mountains (Haxel *et al.*, 1984; Goodwin & Haxel, 1990) (Fig. 1). The Pan Tak Granite intrudes into the Kitt Peak Plutonic Suite, which is part of the Jurassic continental arc system (Haxel *et al.*, 2008; Tosdal & Wooden, 2015; Busby & Centeno-García, 2022). The Kitt Peak Plutonic Suite is generally high-K, calc-alkaline, and metaluminous, and comprises the Aquirre Peak Quartz Diorite (165 to 170 Ma), Kitt Peak Granodiorite (c. 165 Ma), and Pavo Kug Granite (c. 159 Ma) (Haxel *et al.*, 2008). Metamorphosed Paleozoic sedimentary rocks, including metasedimentary schist, calc-silicate schist, marble, and quartzite, are locally exposed as small rafts (<500 m) within the Pan Tak Granite (Fig. 2) but are otherwise not present in the Coyote Mountains (Wright & Haxel, 1982; Haxel *et al.*, 2008). Crystalline basement is also not exposed but is inferred to be the Paleoproterozoic (c. 1.6–1.8 Ga) Pinal block within the larger Mazatzal terrane (Farmer & DePaolo, 1984; Karlstrom & Bowring, 1993). The Pinal block is regionally intruded by Mesoproterozoic (c. 1.4 Ga) granites that have affinities to A-type granites, including the Oracle Granite (Anderson & Morrison, 2005), interpreted to be a potential melt source for the Pan Tak Granite and Wilderness Suite (Wright & Haxel, 1982; Fornash *et al.*, 2013).

The Pan Tak Granite comprises an equigranular, weakly to moderately peraluminous, two-mica ± garnet granite pluton that is intruded by a garnet-muscovite leucogranite, chiefly as dikes and sills (Fig. 3). Wright & Haxel (1982) refer to the equigranular two-mica granite as the 'old phase' and the leucogranite dike network as the 'young phase'. Leucogranite dikes are up to a few tens of meters thick and are predominantly located within the two-mica granite, but locally intrude several kilometers into the Kitt Peak Plutonic Suite. The leucogranite intrudes the two-mica granite in such volume as to be the dominant phase across large (~5 km^2) areas. The leucogranite comprises small intrusive bodies and multiple types of dikes, including aplite dikes, pegmatitic dikes, and granite-textured dikes. The granite-textured dikes, aplitic dikes, and small intrusive bodies crosscut one another and appear to have intruded at approximately the same time. The pegmatitic dikes crosscut all other intrusive units (Fig. 3). Previous studies of the Pan Tak Granite suggested a crystallization age of ~58 Ma for the two-mica granite, including a multi-grain, zircon isotope dilution-thermal ionization mass spectrometry (ID-TIMS), lower concordia intercept age of 58 ± 2 Ma (Wright & Haxel, 1982) and a zircon laser ablation-inductively coupled-mass spectrometry (LA-ICP-MS) age of 58.1 ± 0.5 Ma (Gottardi *et al.*, 2020). The Pan Tak leucogranite has not been previously dated.

ANALYTICAL METHODS

Whole rock powder was analyzed for major and trace elements using ICP-MS and x-ray fluorescence (XRF) spectroscopy at ALS Geochemistry in Reno, NV. Whole rock powder and garnet separates were analyzed for Nd and Sr isotopes using ID-TIMS at the University of Arizona. Oxygen isotope data for quartz, magnetite, muscovite, biotite, and feldspar were measured with isotope ratio mass spectrometry (IRMS) at the High Temperature Stable Isotope Lab at the University of Texas at Austin and is reported relative to Vienna Standard Mean Ocean Water (VSMOW). Zircons were imaged using scanning electron microscope (SEM) backscatter electron (BSE) and cathodoluminescence (CL) detectors and then

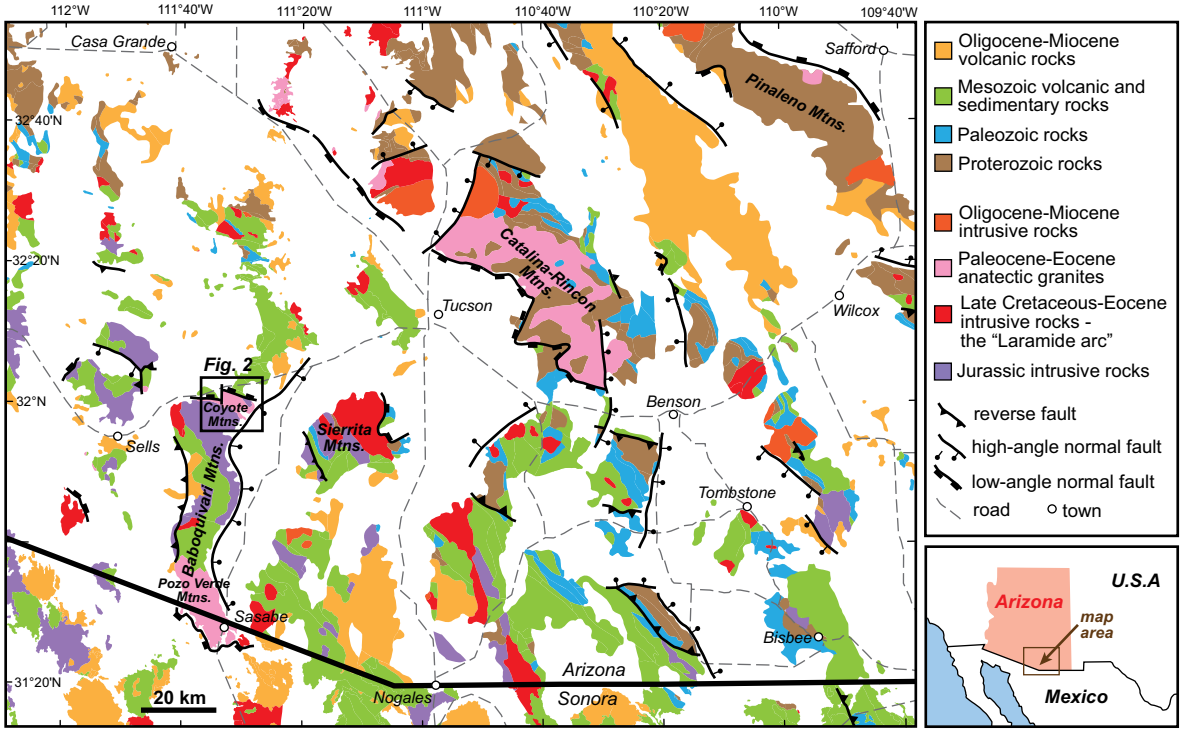

Fig. 1. Regional geologic map of southern Arizona, USA, showing the location of the Pan Tak Granite in the Coyote Mountains and the location of other Paleocene–Eocene anatectic granites in the region.

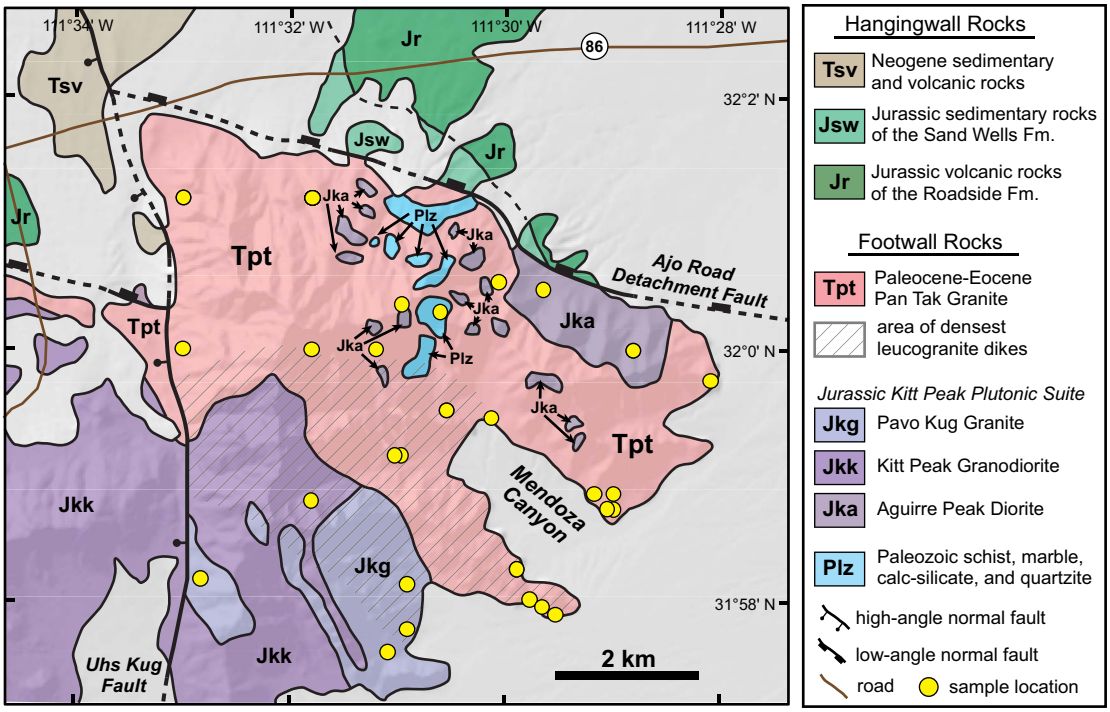

Fig. 2. Detailed geologic map showing the outcrop extent of the Pan Tak Granite and location of samples collected for this study (after Haxel *et al.*, 2008).

analyzed for U–Pb isotopes, trace elements, and Lu-Hf isotopes using LA-ICP-MS at the University of Arizona LaserChron Center. Zircon U–Pb isotopes were also measured with CA-ID-TIMS at the University of Wyoming using two analytical methods. The first method involved analysis of individual zircon fragments after final dissolution. The second method involved multiple analyses at incremental temperature steps that progressively dissolved multiple zircon. A single $^{40}Ar/^{39}Ar$ step-heating analysis was conducted at the University of Vermont Noble Gas Geochronology Lab. A detailed description of all analytical methods employed, including reporting on standards, is presented in Supplementary File 1.

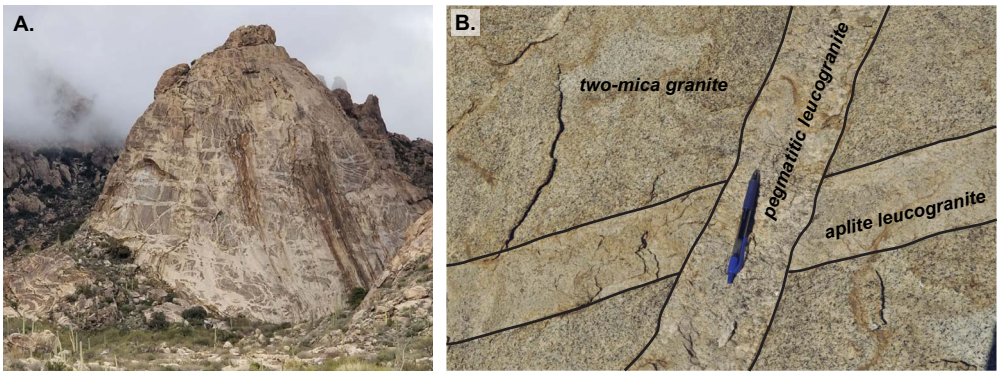

Fig. 3. (A) Photograph of a cliff face (~200 m tall) in Mendoza Canyon in the Coyote Mountains showing intrusive relationships of the Pan Tak Granite. (B) Outcrop photograph showing the two-mica granite intruded by an aplitic leucogranite dike and a pegmatitic leucogranite dike. Pegmatite dikes are the youngest intrusive phase in the Coyote Mountains, based on crosscutting relationships.

RESULTS

Whole rock geochemistry and isotope ratios

Major, minor, and trace element data were measured for 14 samples of two-mica granite, 20 samples of leucogranite, 1 sample of a lamprophyre dike, and 1 sample of the (Jurassic) Pavo Kug Granite from the Kitt Peak Plutonic Suite (Table S1). The two-mica granite is weakly peraluminous, with an average aluminum saturation index (ASI; molar $Al_2O_3/CaO—3.33P_2O_5 + Na_2O + K_2O$) of 1.10. ASI values for the leucogranite range from 1.05 to 1.18 (Fig. 4A). Both phases of the Pan Tak Granite are high silica (72–78 wt % SiO_2) and display sublinear trends on Harker-style diagrams with the leucogranite exhibiting more evolved compositions, including higher SiO_2, Na_2O, and P_2O_5 and lower TiO_2, Fe_2O_3, MgO, and CaO (e.g. Fig. 4B, C). On chondrite-normalized REE diagrams (Fig. 4D), the two-mica granite is moderately enriched in LREE, has flat HREE slope, and has weak negative Eu anomaly. The leucogranite is significantly depleted in LREE, has a prominent negative Eu anomaly (low Eu/Eu*), and displays a range of HREE compositions that reflect modal garnet. Several leucogranite samples display a chondrite-normalized tetrad effect (Irber, 1999; Jahn *et al.*, 2001), with convex-up lanthanide groups (e.g. La to Nd, Gd to Ho, Er to Lu). The Pan Tak Granite is moderately enriched in LILE with lower Sr and Ba contents and higher Rb/Sr in the leucogranite compared to the two-mica granite (Fig. 4E, F).

Whole rock Sr and Nd isotopes were measured for five samples of Pan Tak leucogranite, two samples of Pan Tak two-mica granite, and one sample of Jurassic Aguirre Peak diorite (Table 1). Leucogranite εNd_t values range from −8.3 to −10.6 (average, −9.7), the two-mica granite εNd_t values are −8.3 and − 8.8, and $\varepsilon Nd_t = -4.5$ for the Aguirre Peak diorite sample (Fig. 5). Leucogranite $^{87}Sr/^{86}Sr_i$ values range from 0.709 to 0.717 (average 0.713), the two-mica granite $^{87}Sr/^{86}Sr_i$ values are 0.711 and 0.710, and $^{87}Sr/^{86}Sr_i = 0.706$ for the Aguirre Peak diorite (Fig. 5).

Mineral oxygen isotopes

$\delta^{18}O$ values were measured for quartz, feldspar, biotite, muscovite, magnetite, and garnet from five samples of Pan Tak leucogranite and two samples of two-mica granite (Table 2). Quartz $\delta^{18}O$ values overlap for both phases and range from 9.01 to 9.80‰ (average, 9.30‰). Garnet $\delta^{18}O$ values for both phases range from 5.37 to 5.54‰ (average 5.43‰).

Zircon textures

The intrusive units of the Pan Tak Granite have distinctive zircon textures. Zircons from pegmatite dikes are subhedral, relatively large (200–500 μm long), and do not display any internal structure such as zoning or inherited cores (Fig. 6A). These zircons have a spongy, metamict texture made up of numerous microscale (≤10 μm) pores and mineral inclusions. Larger inclusions, up to 50 μm, are present in some grains. Zircons from granite-textured leucogranite dikes are similar to the pegmatite dike zircons but are smaller (100–300 μm long) and contain relicts of oscillatory zoning that have been overprinted by the development of micro-porosity and spongy texture (Fig. 6B). There are no clear rim–core structural relationships or other evidence for inherited (xenocrystic or antecrystic) components. Zircons from the aplite leucogranite dikes are similar to the granite-textured dikes but are smaller (50–200 μm long), and the microporous, spongy domains are limited to zircon interiors (Fig. 6C, D). These domains are surrounded by oscillatory zoned zircon. Localized overprinting of oscillatory zoning and the presence of fractures (Fig. 6D) suggest the zircon interiors were altered after the oscillatory zones crystallized. The finely spaced oscillatory zoning is locally convoluted (Fig. 6D). The oscillatory/convoluted zoning and spongy texture in zircons from the aplite dikes are both discordantly crosscut by irregularly shaped domains of relatively homogenous, low-U zircon, characterized by a bright CL response (Fig. 6D, top right of crystal).

Zircons from the two-mica granite contain abundant inherited xenocrystic cores and lack spongy textures characterized by abundant mineral inclusions (Fig. 6E–I). Several zircons investigated display patchy, lobate, and amoeboid textures in their interiors, surrounded by oscillatory zoned domains (Fig. 6E, F). The patchy textures consist of bright CL (low-U) recrystallized domains that replaced primary, dark CL (high-U) zircon interiors. Although the unusual patchy to lobate textures in the two-mica granite zircons are conspicuous, a large majority of zircon interiors (>90%) display ordinary oscillatory or sector zoning (Fig. 6G, H). The zoned domains and patchy texture domains are surrounded by thin (≤10 μm), dark CL, zircon overgrowths (i.e. 'rims') that display oscillatory zoning and locally replace and crosscut the pre-existing crystalline structure (Fig. 6E–H).

Geochronology

For the two-mica granite, LA-ICP-MS zircon U–Pb dates were obtained from samples CM-246, CM-218, and CM-214 (Table S2). There are two major $^{206}Pb/^{238}U$ age populations, centered on ~58 and ~166 Ma (Fig. 7A, B). The Jurassic age population predominately reflects analyses of zircon cores. The Paleocene–Eocene age population shows an inverse linear relationship between zircon U–Pb date and U concentration (Fig. 8A). After discarding

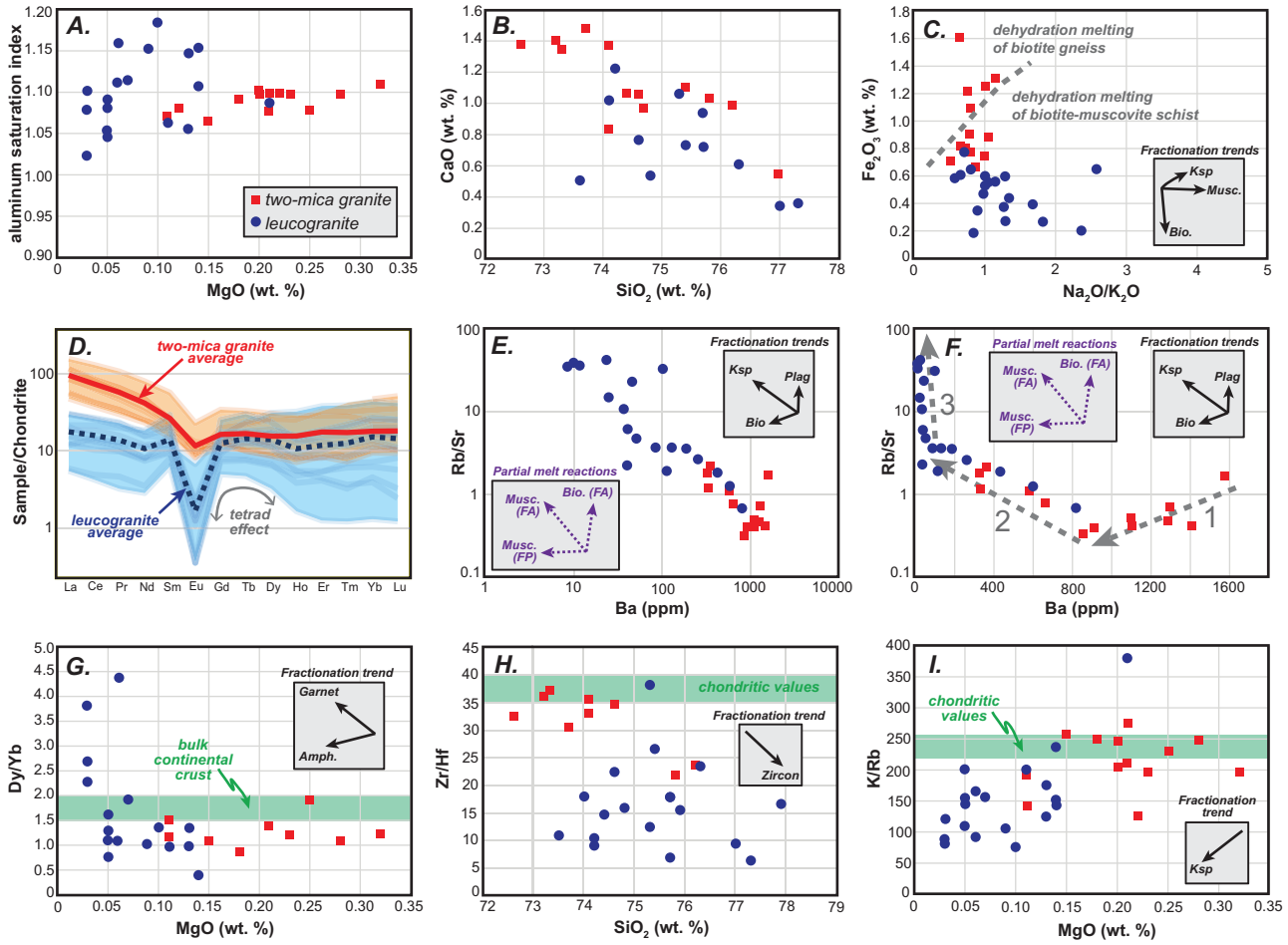

Fig. 4. Whole rock geochemical data from the Pan Tak Granite. (A) Aluminum saturation index plotted against MgO. (B) CaO plotted against SiO_2. (C) Fe_2O_3 plotted against Na_2O/K_2O. Dehydration melting fields from Weinberg & Hasalová (2015) and mineral fractionation trends calculated using the method of Jagoutz (2010). (D) Chondrite normalized (McDonough & Sun, 1995) rare earth element data. (E, F) Rb/Sr plotted against Ba. Melt reaction trends and fractionation trends are from Inger & Harris (1993). (G) Dy/Yb plotted against MgO. Bulk continental crust values and fractionation trends are from Davidson *et al.* (2013). (H) Zr/Hf plotted against SiO_2. Chondritic values and fractionation trends are from Claiborne *et al.* (2006). (I) K/Rb plotted against SiO_2. Chondritic values and fractionation trends are from Blevin (2004).

Table 1: Rb–Sr and Sm–Nd isotopic compositions of the Pan Tak Granite and Aguirre Peak diorite. WR= whole rock.

Sample	Type	Latitude (°N)	Longitude (°W)	$^{147}Sm/^{144}Nd$	$^{143}Nd/^{144}Nd_{(0)}$	$^{143}Nd/^{144}Nd_{(t)}$	$\varepsilon Nd_{(t)}$	$^{87}Rb/^{86}Sr$	$^{87}Sr/^{86}Sr_{(0)}$	$^{87}Sr/^{86}Sr_{(i)}$
Pan Tak: two-mica granite										
CM-246	WR	31.992	111.509	0.128718	0.512188	0.512142	−8.3	4.389609	0.713761	0.710331
CM-252	WR	31.966	111.494	0.134407	0.512165	0.512117	−8.8	5.315005	0.715394	0.711241
Pan Tak: leucogranite										
CM-9	WR	31.986	111.516	0.23005	0.512128	0.512053	−10.2	34.856251	0.738298	0.713541
CM-11a	WR	31.986	111.517	0.189277	0.512208	0.512146	−8.3	3.029359	0.711486	0.709334
CM-248	WR	31.992	111.509	0.336517	0.512147	0.512037	−10.5	8.906962	0.718855	0.712529
CM-224	WR	31.995	111.467	0.183452	0.512088	0.512033	−10.7	4.252525	0.720181	0.717161
CM-224	Garnet	31.995	111.467	1.083661	0.512362	0.512036	−10.6			
CM-256	WR	32.005	111.51	0.134407	0.512165	0.512125	−8.9			
CM-256	Garnet	32.005	111.51	0.72198	0.512346	0.512129	−8.8			
Aguirre Peak diorite										
CM-260	WR	32.008	111.494	0.111884	0.512316	0.512195	−4.5	0.424458	0.707256	0.706260

strongly discordant (>20%) and reverse discordant (>5%) data, calculated according to Gehrels (2012), these dates range from 42 to 62 Ma. Three discordant analyses from the two-mica granite have Paleozoic to Proterozoic dates and yield an upper intercept of 1420 ± 20 Ma (2σ) on a Wetherill concordia plot (Fig. 7C), which overlaps with the approximate crystallization age of the Oracle Granite (Fornash *et al.*, 2013). LA-ICP-MS zircon dates were obtained from leucogranite samples CM-208, CM-224, and CM-248 and likewise display an inverse relationship between zircon U–Pb date and U concentration. Concordant zircon U–Pb dates from the

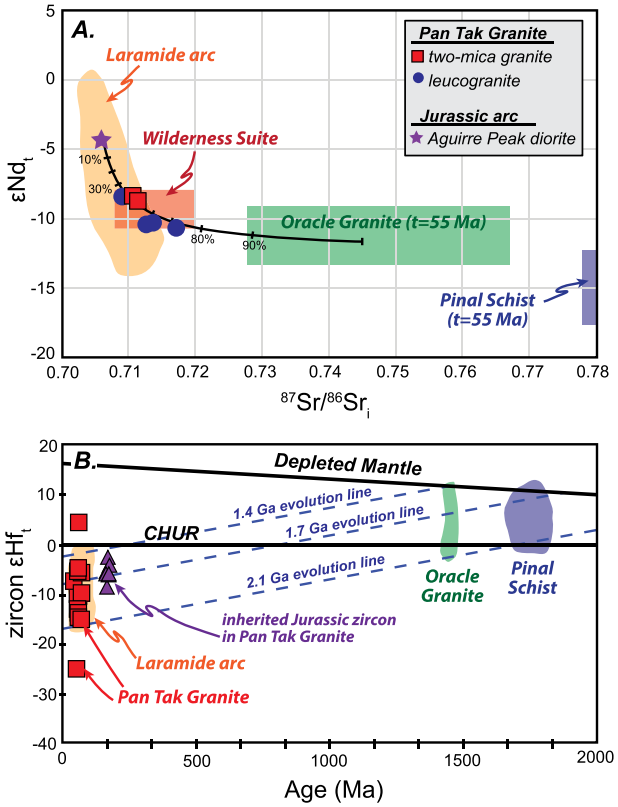

Fig. 5. (A) Whole rock Sm–Nd and Rb–Sr isotopic compositions for the Pan Tak Granite. Data fields for the Laramide arc, Wilderness Suite, Oracle Granite, and Pinal Schist are presented in Scoggin *et al.* (2021). Mixing line shows percentage mixing between the Aguirre Peak diorite (sample CM-260) and an average Oracle Granite (see text for details). (B) Single grain zircon Lu-Hf isotopic compositions from the Pan Tak two-mica granite. Data fields for the Laramide arc, Oracle Granite and Pinal Schist are adapted from Fornash *et al.* (2013) and Scoggin *et al.* (2021).

leucogranite range from 41 to 48 Ma. All but two analyses from samples CM-224 (granite-textured dike) and CM-248 (pegmatite dike) produced strongly discordant or otherwise unreliable U–Pb data (e.g. anomalously low $^{206}Pb/^{204}Pb$). Considering all concordant zircon LA-ICP-MS ages from the two-mica granite and leucogranite together, there is an apparent age gap (discussed below) from about 51 to 53 Ma (Fig. 7B).

Zircons from leucogranite sample CM-256 were analyzed for U–Pb by ID-TIMS (Table S3). Two individual zircons that were not chemically abraded yielded concordant $^{206}Pb/^{238}U$ dates of 39.14 ± 1.35 (2σ) and 53.95 ± 0.41 (2σ). For the two-step chemical abrasion analysis, eight individual zircon shards yielded concordant $^{206}Pb/^{238}U$ dates ranging from 53.3 to 59.4 Ma, and one shard yielded a concordant date of 94.91 ± 0.35 (2σ) (Fig. 7D). The multi-grain, multi-step chemical abrasion analysis yielded steps with concordant $^{206}Pb/^{238}U$ dates ranging from 38.1 to 55.0 Ma. The last five (of seven) step dates were within error of one another and result in a weighted mean date of 54.93 ± 0.04 (2σ, mean squared weighted deviation (MSWD) = 0.84) (Fig. 7D).

Sm–Nd isotopes were measured for whole rock and garnet separates from leucogranite samples CM-224 and CM-256, both granite-textured dikes (Table 1). Two-point isochrons, or 'tie lines', yield dates of 47.1 ± 1.6 Ma (2σ) for sample CM-224 and 46.5 ± 1.2 Ma (2σ) for sample CM-256 (Fig. 7E). Biotite was analyzed for $^{40}Ar/^{39}Ar$ from sample CM-302, a lamprophyre dike that crosscuts all leucogranite units. The lamprophyre dike yielded a plateau date of 25.92 ± 0.52 Ma (2σ) (Fig. 7F), consistent with intrusion during crustal extension that formed the Coyote Mountains metamorphic complex (Gottardi *et al.*, 2020). The intrusion of the lamprophyre dike and the extensional deformation that formed the Coyote Mountains metamorphic complex are significantly younger than the Pan Tak Granite.

Zircon geochemistry and Lu-Hf isotopes

Zircon trace element concentrations were measured from two-mica granite samples CM-246, CM-218, and CM-214 and from leucogranite sample CM-208, an aplite dike. Data are reported only from zircons that yielded concordant U–Pb dates (Table S4). Leucogranite zircons contain higher Hf concentrations and higher U/Th (Fig. 8B, C) compared to two-mica granite zircons. Zircon REE concentrations overlap between two-mica granite and leucogranite samples, although temporal trends are apparent when data are plotted against zircon U–Pb date. Eu/Eu* $[Eu_n/((Sm_n + Gd_n)/2]$ decreases with decreasing date (Fig. 8D). All zircon REE increase with decreasing date for the two-mica granite (from ~62 Ma to the age gap) (represented by Yb_n in Fig. 8E), with MREE/HREE relatively constant (represented by Dy_n/Yb_n in Fig. 8F) and LREE/MREE increasing markedly (represented by Nd_n/Dy_n in Fig. 8F). For the leucogranite (from the age gap to ~42 Ma), LREE and HREE decrease with decreasing zircon U–Pb date and MREE remains relatively constant (Fig. 8E). MREE/HREE increases during this time interval and LREE/HREE decreases (Fig. 8F).

Melt crystallization temperatures were estimated using a version of the Ti-in-zircon thermometer ($T_{Ti\text{-}zr}$) of Ferry & Watson (2007) that was updated by Loucks *et al.* (2020) to include pressure. Yang *et al.* (2022) reported a crystallization pressure of 704 ± 37 MPa for the Pan Tak Granite, which is the only pressure estimate available. Following the recommendation of Schiller & Finger (2019), we used rhyolite-MELTS (Gualda *et al.*, 2012) to calculate aSiO and aTiO$_2$ at 750 °C and 700 MPa for the average composition of the Pan Tak two-mica granite, assuming a water content of 3 wt %. The calculated values are $aSiO_2 = 1$ and $aTiO_2 = 0.55$, which are similar to the activities reported by Schiller & Finger (2019) for high-silica S-type granites that lack major Ti-bearing phases (e.g. titanite, rutile). Compared to a rutile saturated melt ($aTiO_2 = 1$), using $aTiO_2 = 0.55$ increases $T_{Ti\text{-}zr}$ by ~50 °C. Using the pressure-dependent $T_{Ti\text{-}zr}$ equation from Loucks *et al.* (2020) increases $T_{Ti\text{-}zr}$ by ~30 °C, compared to the original equation from Ferry & Watson (2007). Two-mica granite samples CM-246, CM-218, and CM-214 have average $T_{Ti\text{-}zr} = 782 \pm 40$, 761 ± 23, and 848 ± 16 °C, respectively, with uncertainty reported as one standard error. Average $T_{Ti\text{-}zr}$ for leucogranite sample CM-208 is 710 ± 34 °C. When plotted against zircon U–Pb age, $T_{Ti\text{-}zr}$ increases from ~650 to ~850 °C from 62 Ma to the age gap (53–51 Ma) and then decreases to ~650 °C at the end of the crystallization sequence at 42–44 Ma (Fig. 8G).

Lu-Hf isotopes were measured on zircons from two samples of the Pan Tak two-mica granite (Table S5). Analyses included Paleocene–Eocene (magmatic) zircons and Jurassic (inherited xenocrystic) zircons. Sample CM-246 yielded individual Paleocene–Eocene εHf_t values ranging from −26.1 to −8.2 with an average of -14.7 ± 3.2 (2σ, $n = 5$), with uncertainty calculated by adding standard error and average individual error in quadrature. Sample CM-218 yielded individual Paleocene–Eocene εHf_t values ranging from −14.9 to −4.6 with an average of -9.7 ± 2.1 (2σ, $n = 6$). All Paleocene–Eocene zircon analyses combined yield an average of $\varepsilon Hf_t = -12.0 \pm 2.1$ (2σ, $n = 11$), and all Jurassic analyses combined yield an average of $\varepsilon Hf_t = -5.4 \pm 1.4$ (2σ, $n = 7$). Zircon

Table 2: Oxygen isotopic composition for select minerals of the Pan Tak Granite

Sample	Latitude (°N)	Longitude (°W)	Quartz $\delta^{18}O$	Biotite $\delta^{18}O$	Muscovite $\delta^{18}O$	Feldspar $\delta^{18}O$	Magnetite $\delta^{18}O$	Garnet $\delta^{18}O$
Pan Tak: two-mica granite								
CM-252	31.966	111.494	9.04				0.58	5.37
CM-209	31.971	111.498	9.8	5.69			3.11	
Pan Tak: leucogranite								
CM-216	31.981	111.486	9.01					
CM-225	31.995	111.467	9.15					
CM-228	31.963	111.515	9.15		6.52		0.09	5.38
CM-242	31.991	111.502	9.5					
CM-248	31.992	111.509	9.42		6.71	6.68		5.54

All $\delta^{18}O$ values are reported in ‰ relative to VSMOW.

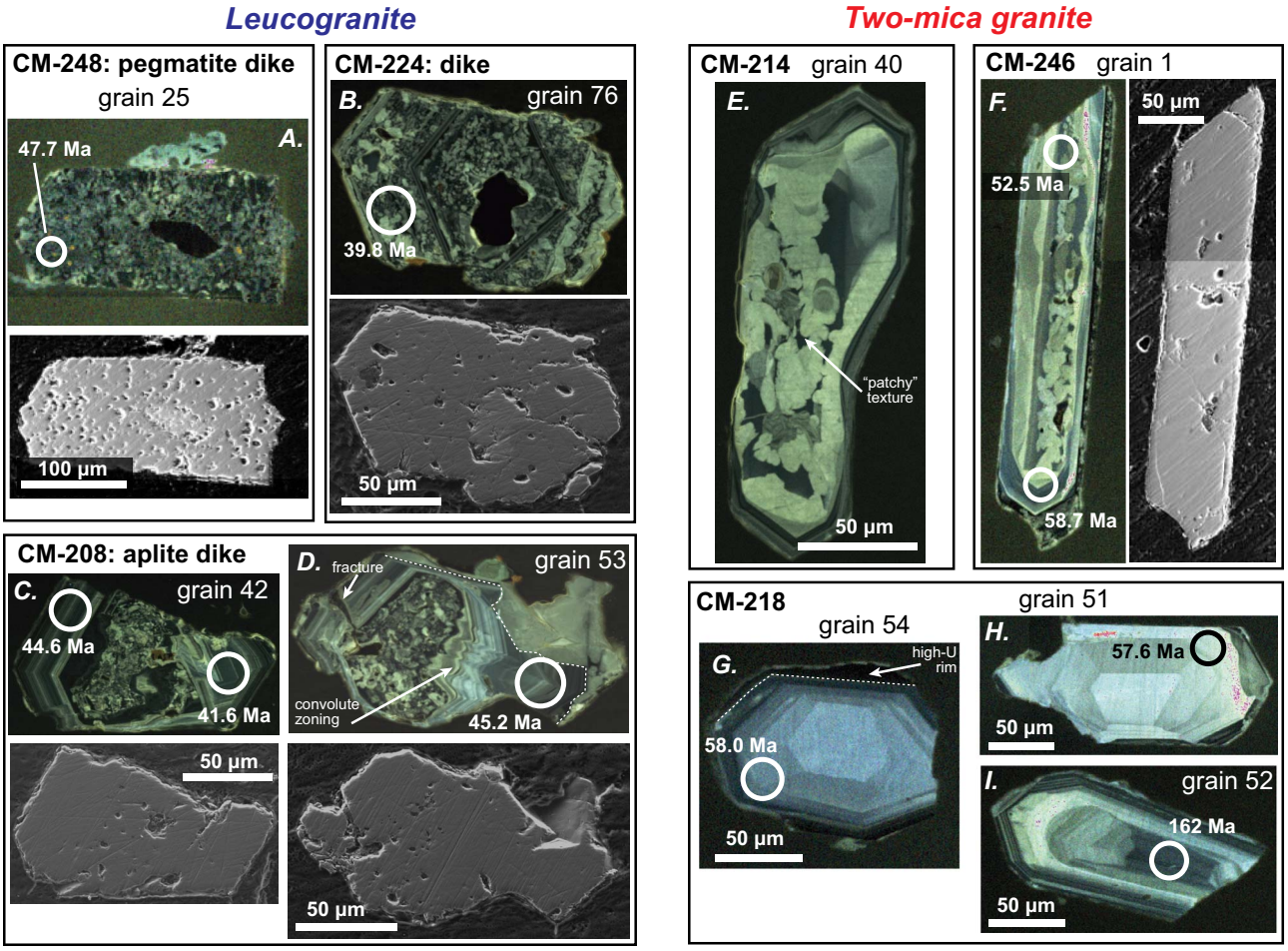

Fig. 6. Representative color CL images and grayscale secondary electron (SE) images of zircons from samples of the Pan Tak leucogranite dikes (panels A–D) and from the Pan Tak two-mica granite (panels E–I). White circles with dates are 30-micron LA-ICP-MS spots.

εHf_t and U–Pb ages from the Pan Tak Granite overlap isotopic data from the Wilderness Suite (Fornash *et al.*, 2013; Ducea *et al.*, 2020) and primarily plots along 1.4 to 2.1 Ga crustal evolution lines (Lu/Hf = 0.015) that intercept zircon εHf_t values from the Laramide arc, Jurassic granitoids, Oracle Granite, and Pinal Schist (Fig. 5), all possible protoliths of the Pan Tak Granite.

DISCUSSION

Melt sources

Abundant Jurassic-age zircon cores are present in the two-mica granite (Fig. 6I), inherited from Jurassic granitoids rocks of the type that the Pan Tak Granite intrudes (Haxel *et al.*, 2008). Despite the abundance of inherited zircons of Jurassic age, zircon εHf_t and whole rock εNd_t and $^{87}Sr/^{86}Sr_i$ values require the involvement of older and more radiogenically evolved sources (Fig. 5). Proterozoic basement rocks exposed in the region include a diabase dike swarm (1.1 Ga), Oracle Granite (c. 1.4 Ga), and Pinal Schist (c. 1.6–1.8 Ga) (Anderson & Bender, 1989; Bright *et al.*, 2014; Meijer, 2014). Three zircon U–Pb LA-ICP-MS analyses from the two-mica granite define a discordia with a 1.42-Ga upper intercept age (Fig. 7C), and six zircon size fractions analyzed by TIMS by Wright & Haxel (1982) have an upper concordia intercept age of 1.1 Ga. Gottardi *et al.* (2020) report two Proterozoic zircon U–Pb LA-ICP-MS dates,

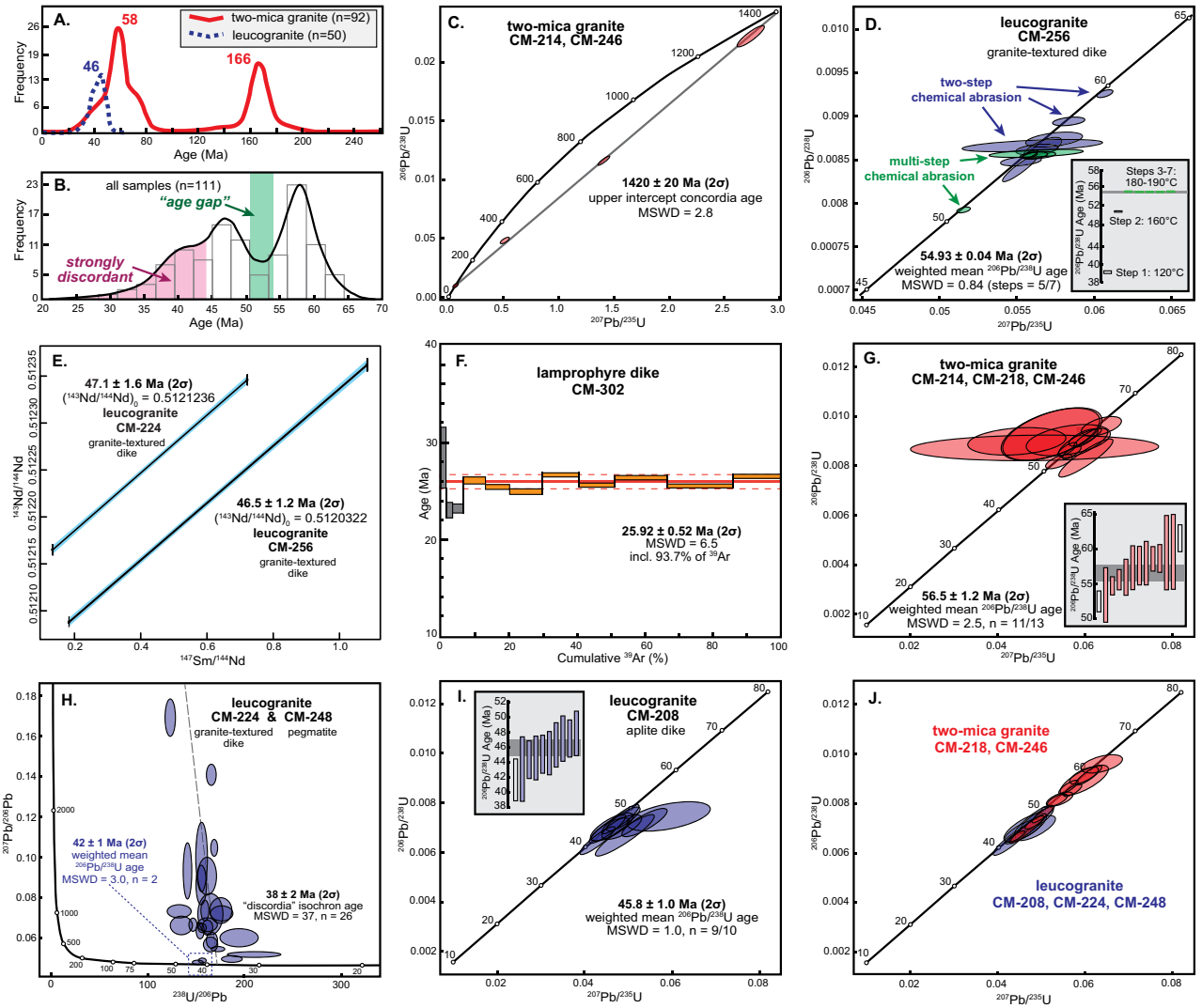

Fig. 7. Geochronology data from the Pan Tak Granite. (A) Kernel density estimate (KDE) of zircon U–Pb LA-ICP-MS data from the two-mica granite and leucogranite. Note the absence of older ages for the leucogranite samples. (B) KDE and histogram of zircon U–Pb LA-ICP-MS data from the Pan Tak Granite showing the age gap from approximately 53–51 Ma. Ages younger than ~42 Ma are discordant and interpreted to have experienced Pb loss or other disruptions to the U–Pb system. (C) Wetherill concordia with zircon LA-ICP-MS data from the two-mica granite, showing inherited components with an upper intercept age of ~1420 Ma. (D) Zircon U–Pb ID-TIMS data from leucogranite sample CM-256 plotted on a Wetherill concordia diagram. The weighted mean age of ~55 Ma is from the last five steps of the multi-step analysis. (E) Two-point Sm–Nd tie lines (isochrons) for whole rock and garnet separate from leucogranite samples. (F) Ar release spectra for lamprophyre dike sample CM-302. Steps highlighted were used to define a plateau age of ~26 Ma. (G) Zircon U–Pb LA-ICP-MS data from the two-mica granite, plotted on a Wetherill concordia after discarding outliers, analyses of zircons that show textural evidence for alteration and have U > 10 000 ppm. (H) Zircon U–Pb LA-ICP-MS data from leucogranite dikes, plotted on a Tera–Wasserburg concordia showing that almost all analyses from granite-textured and pegmatitic dikes are discordant. Both ages presented are interpreted to underestimate the age of the leucogranite dikes due to Pb loss or other disruptions to the U–Pb system. (I) Zircon U–Pb LA-ICP-MS data from a leucogranite aplite dike, plotted on a Wetherill concordia after discarding outliers, analyses of zircon that show textural evidence for alteration and have U > 5000 ppm. (J) Zircon U–Pb LA-ICP-MS data from all samples of the Pan Tak Granite, plotted on a Wetherill concordia. Only low-error data that are concordant from zircons with no textural evidence for alteration or metamictization are shown. The analyses define a spectrum of ages from 62 to 42 Ma.

1.11 Ga and 1.47 Ga, from the Pan Tak two-mica granite. Proterozoic zircon components could have been recycled from Jurassic igneous rocks, but inherited Proterozoic zircon ages are uncommon in Jurassic granitoids rocks (Tosdal & Wooden, 2015). Scoggin *et al.* (2021) suggested that the 1.1-Ga diabase dikes, or other Proterozoic mafic igneous rocks, could be a potential source for the anatectic Relleno Suite in the Piñaleno Mountains. However, the whole rock geochemistry (e.g. $SiO_2 = 65–75$ wt %; ASI < 1.1) and isotopic composition (e.g. quartz $\delta^{18}O_{VSMOW} < 9.5‰$; $^{87}Sr/^{86}Sr_i < 0.71$; zircon $\varepsilon Hf_t > -8$) of the Relleno Suite that supported this interpretation are not observed in the Pan Tak Granite. By contrast, the geochemical and isotopic composition of the Pan Tak Granite is most similar to the Wilderness Suite (Keith *et al.*, 1980; Fornash *et al.*, 2013; Ducea *et al.*, 2020) (Fig. 5). Fornash *et al.* (2013) favored the Oracle Granite as a main source for the Wilderness Suite, based in part on numerous c. 1.4 Ga inherited zircon cores. Wright & Haxel (1982) also favored the Oracle Granite as a source for the Pan Tak Granite. Quartz $\delta^{18}O_{VSMOW}$ from the Pan Tak Granite (9.0–9.8‰) is more similar to Oracle Granite (9 to 11‰) than it is to the Pinal Schist (>12‰) (Turi & Taylor, 1971; Kerrich & Rehrig, 1987; Anderson & Morrison, 2005). Some experimental studies have suggested that weakly peraluminous melt compositions and moderate Fe and Mg melt contents, similar to the Pan Tak two-mica granite (ASI, 1.05 to 1.1), disfavor a significant felsic

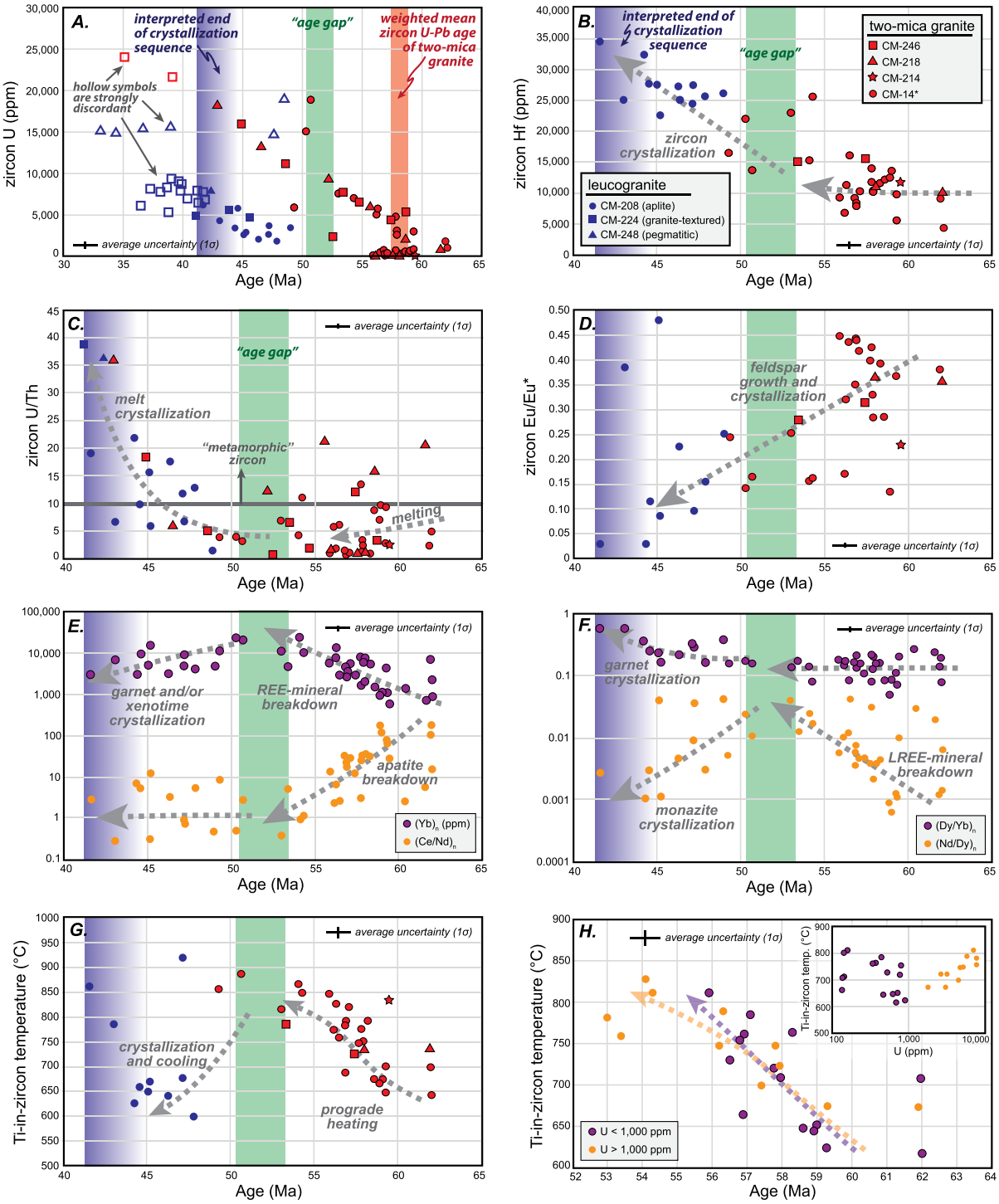

Fig. 8. Zircon trace element data plotted against zircon U–Pb date. Explanation of symbols are presented in panel B unless otherwise specified. (A) Zircon U concentration plotted against date showing sublinear trends of increasing U concentrations with decreasing age. Open symbols represent strongly discordant (>20%) analyses. The weighted mean age of the two-mica granite (red bar) is from Fig. 7G, the age gap (green bar) is from Fig. 7B, and the end of the crystallization sequence (blue bar) is interpreted from the youngest concordant zircon U–Pb analyses from the leucogranite. (B) Zircon Hf concentrations plotted against date. Gray dashed arrows are interpreted trends in all panels and are not regressed through data. (C) Zircon U/Th ratios plotted against date. (D) Zircon Eu/Eu∗ ($Eu_n/((Sm_n + Gd_n)/2)$) plotted against date, where n denotes normalization to chondrite values from McDonough & Sun (1995). (E) Zircon Yb_n and $(Ce/Nd)_n$ plotted against date. (F) Zircon $(Dy/Yb)_n$ and $(Nd/Dy)_n$ plotted against date. (G) Ti-in-zircon temperature ($T_{Ti\text{-}zr}$) estimates plotted against date. (H) Same as panel G, but with zircon distinguished by U content. Inset plots zircon $T_{Ti\text{-}zr}$ against zircon U content.

metasedimentary source (cf. Patiño-Douce, 1999) (Fig. 4A, C). However, phase equilibria modeling and studies of nanogranitoids suggest that ASI, Fe, and Mg may be artificially enriched in experimental crustal melts and that high ASI, Fe, and Mg is not necessarily indicative of metasedimentary protoliths (Bartoli, 2021; Bartoli & Carvalho, 2021). Simple binary mixing between the Aguirre Peak Quartz Diorite and average Oracle Granite Sr and Nd isotope ratios (Barovich, 1991) suggests that 40–70% of Oracle

Granite may have been involved in melting (Fig. 5). The exact source for the Pan Tak Granite remains uncertain but is estimated to consist of subequal proportions of Jurassic granitoids and Proterozoic basement, predominantly Oracle Granite or equivalent.

Age interpretations

Two-mica granite

Excluding analyses of inherited xenocrystic zircons and strongly discordant or reverse discordant analyses (Gehrels, 2012), zircon LA-ICP-MS data from the two-mica granite display a semi-continuous range of $^{206}Pb/^{238}U$ dates from 42 to 62 Ma (Figs 7 and 8). Analogous ranges of zircon dates have been observed in other anatectic granites in southern Arizona, including the Wilderness Suite (34–64 Ma; Davis *et al.*, 2019) and in many Himalayan leucogranites (Kohn, 2014; Weinberg, 2016; Wu *et al.*, 2020). How to interpret this spread of zircon U–Pb dates is one of the challenges associated with anatectic leucogranites, regardless of their location or tectonic association. For the Pan Tak two-mica granite, there is an inverse linear relationship between zircon U–Pb date and zircon U concentration (Fig. 8A). One interpretation of this trend is that radiation damage of the zircon matrix is proportional to U concentration (Ewing *et al.*, 2003) and that younger ages reflect Pb loss. Regression of a line through the age-U trends in Fig. 8A–U, ≤5000 ppm, suggests a crystallization age of 57–62 Ma. Only considering zircon data that are (1) concordant, (2) do not display textural evidence for metamictization, diffusion–reaction, or dissolution–reprecipitation processes, (3) have moderate to low U concentrations (<10 000 ppm), and (4) have U–Pb dates that overlap within error yields a weighted mean $^{206}Pb/^{238}U$ date of 56.5 ± 1.2 Ma (2σ; $n = 11$) (Fig. 7G). Further restricting the data to zircons with U concentrations <3000 ppm yields a weighted mean date of 57.9 ± 1.1 Ma (2σ, $n = 6$). These ages overlap within error with a previously reported zircon U–Pb ID-TIMS date of 58 ± 2 Ma (Wright & Haxel, 1982) and a zircon LA-ICP-MS date of 58.1 ± 0.5 Ma (Gottardi *et al.*, 2020). The most conservative interpretation of these dates is that they reflect a single episode of crystallization of the Pan Tak two-mica granite at c. 58 Ma. However, several lines of evidence lead us to propose a more complex crystallization history and to suggest that the range in zircon U–Pb dates has geologic significance (see Crystallization sequence section below).

Leucogranite

No age has been previously reported for intrusion of the Pan Tak leucogranite. Crosscutting relationships indicate that the leucogranite is younger than the two-mica granite and that pegmatitic dikes are younger than granite-textured and aplitic leucogranite dikes (Fig. 3B). Like the two-mica granite, zircon U–Pb LA-ICP-MS data from the Pan Tak leucogranite display an inverse linear relationship between date and U concentration (Fig. 8A). High U (>5000 ppm) zircons are generally discordant and show evidence for loss of radiogenic Pb and metamictization. The spongy, microporous texture and abundance of small mineral inclusion in zircons from pegmatite dike sample CM-248 and granite-textured leucogranite dike sample CM-224 (Fig. 6A, B) are indicative of diffusion–reaction processes mediated by aqueous fluids (Tomaschek *et al.*, 2003; Geisler *et al.*, 2007; Nasdala *et al.*, 2010; Park *et al.*, 2016). These textures are generally limited to zircons that have experienced structural damage due to self-irradiation and are commonly observed in felsic pegmatites (e.g. Van Lichtervelde *et al.*, 2009; Soman *et al.*, 2010; Zamyatin *et al.*, 2017; Budzyń *et al.*, 2018). Not enough concordant zircon U–Pb LA-ICP-MS data were obtained from samples CM-248 and CM-224 to calculate a weighted mean age; however, we can place some constraints on crystallization ages. Forcing a 'discordia' isochron through the discordant LA-ICP-MS data from these two samples on a Tera–Wasserburg diagram using modern common Pb values yields a date of ~38 Ma, which can be considered a minimum age (Fig. 7H). Considering only the least discordant data from these two samples suggests a date of 42 ± 2 Ma (2σ, $n = 2$), which can also be considered a minimum age.

Like the pegmatite and granite-textured leucogranite units, zircons from the aplite dike sample CM-208 contain microporous, spongy domains interpreted to be related to metamictization. However, these domains are limited to zircon interiors (Fig. 6C, D), which are surrounded by oscillatory and sector zoned domains that appear to be free of alteration, have relatively low U concentrations (generally <5000 ppm), and yielded concordant zircon U–Pb LA-ICP-MS dates (Fig. 7I). LA-ICP-MS U–Pb data collected from these domains were concordant and yielded a weighted mean $^{206}Pb/^{238}U$ date of 45.8 ± 1.0 Ma (2σ; $n = 9$) (Fig. 7I), which we interpret to be the approximate timing of zircon crystallization. This age is within error of the Sm–Nd, garnet-whole rock isochron (tie line) dates for two separate granite-textured leucogranite dike samples, CM-224 and CM-256 (Fig. 7E). Textural observations suggest that the high-U zircon interiors in sample CM-208 were preferentially altered by hydrous fluids that accessed the interiors through fractures (Fig. 6D), which are common in metamict zircons (Krogh & Davis, 1975; Nasdala *et al.*, 2010).

Leucogranite sample CM-256 also was analyzed by CA-ID-TIMS. One zircon not chemically abraded and eight chemically abraded zircon shards from the two-step analysis yielded a cluster of concordant $^{206}Pb/^{238}U$ dates 53–59 Ma. We interpret this variation to reflect minor amounts of uncorrected Pb loss and minor inheritance. The last five (of seven) steps from the multi-grain analysis yielded a concordant weighted mean $^{206}Pb/^{238}U$ date of 54.93 ± 0.04 Ma. This date is older than the Sm–Nd garnet-whole rock isochron age from the same sample and older than zircon LA-ICP-MS dates from other leucogranite samples, but similar to the dominant age population in the two-mica granite. *In situ* LA-ICP-MS analyses of zircons from other granite-textured leucogranite dikes indicate that young (<53 Ma) domains have high U concentrations (>5000 ppm) and display textural evidence for metamictization and alteration (Fig. 6B). Although several studies have noted the preferential dissolution of high-U, young, exterior zircon domains during chemical abrasion (e.g. Curry *et al.*, 2021), we do not see evidence of an age bias in our data from CM-256. The c. 55 Ma date shows up in the third step of the multi-step analysis when the extracted U abundances were very high (25 ng, 20% of the total; Table S3) and persist through two more steps of high U extractions and two steps of lower U extractions. The pattern of young dates in the early dissolution steps followed by a plateau of consistent older dates from all later steps (Fig. 7D, inset) fits the well-defined pattern of multiple-step chemical abrasion described by Mattinson (2005) for magmatic zircons. In Mattinson's study, the young dates were interpreted to reflect preferential early dissolution of metamict domains that had lost Pb. We interpret the 53- to 59-Ma CA-ID-TIMS dates from CM-256 to represent analyses of antecrystic zircons that were inherited from the two-mica granite, and that the magmatic age of this leucogranite sample is better estimated by the Sm–Nd data than the zircon data.

Crystallization sequence

A significant population of zircons from the Pan Tak Granite have relatively young (mostly <42 Ma) LA-ICP-MS dates that are

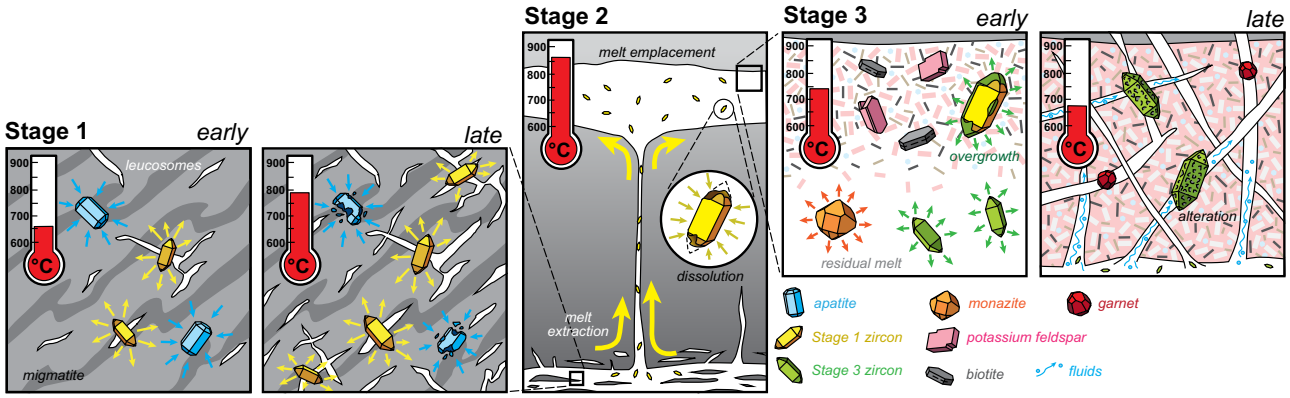

Fig. 9. Schematic cartoon showing the interpreted melt history and crystallization sequence of the Pan Tak Granite. See text for discussion.

strongly discordant, have high U concentrations (>5000 ppm), and display textural evidence for metamictizaiton or alteration (Fig. 6A, B). These zircons are interpreted to have experienced significant Pb loss and are not considered further (hollow symbols in Fig. 8A). The remaining zircon U–Pb LA-ICP-MS analyses from the two-mica granite and leucogranite are concordant (Fig. 7J), and the zircons do not exhibit textural evidence for metamictizaiton or alteration (Fig. 6C–I); however, U concentrations are still quite high, in some cases exceeding 1 wt %. It is unclear whether these zircons have experienced Pb loss. We rule out mechanical mixing (e.g. ablation spot overlapping age domains) because (1) there are no time/depth-dependent variations in the isotopic signals during analyses, (2) comparison of post-ablation images with pre-ablation CL images suggests analyses were conducted within a single age domain, and (3) zircon trace element trends (Fig. 8) cannot be reproduced by simple binary mixing. We interpret the range of LA-ICP-MS dates (42–62 Ma) and ID-TIMS dates (53–59 Ma) to reflect prolonged igneous crystallization and fluid/melt-mediated recrystallization that collectively define a crystallization sequence. Supporting this interpretation are zircon geochemical and temporal trends that record details of melt evolution and changing conditions of crystallization conditions.

The proposed crystallization sequence consists of three stages: (1) metamorphism and melt generation 62–53 Ma, (2) peak metamorphism and melt extraction 53–51 Ma, and (3) cooling and crystallization 51–42 Ma (Fig. 9). During stage 1, from approximately 62 to 53 Ma, the source region experienced metamorphism, anatexis, and zircon (re)crystallization. Increasing $T_{Ti\text{-}zr}$ (from 650 to 850 °C) is interpreted to represent a period of prograde metamorphism during stage 1. Previous studies of silicic volcanic series have documented a negative correlation between zircon Ti and U content for zircon U < ~1000 ppm and a positive correlation for zircon U > ~1000 ppm (e.g. Chamberlain *et al.*, 2014; Matthews *et al.*, 2015; Troch *et al.*, 2018), which is also observed in zircons from the Pan Tak two-mica granite (Fig. 8H, inset). Troch *et al.* (2018) suggested that substitution of non-stoichiometric trace elements in high U zircon distorts the crystal lattice and can facilitate substitution of the slightly larger (compared to Si) Ti^{4+} ion, potentially causing $T_{Ti\text{-}zr}$ to be overestimated. For the Pan Tak two-mica granite, increasing $T_{Ti\text{-}zr}$ during stage 1 is observed for both high U (>1000 ppm) and low U (<1000 ppm) zircon (Fig. 8H). Caution in interpreting the $T_{Ti\text{-}zr}$ vs age trends (Fig. 8G) in the Pan Tak Granite is still warranted, but the similar temporal trends for both high and low U zircon give us more confidence that the stage 1 trend is robust.

The increasing zircon REE concentrations during stage 1 are interpreted to represent breakdown of REE-bearing minerals in the source (Fig. 8E, F). Relatively invariant $(Dy/Yb)_n$ during this interval suggests a limited role for garnet (e.g. Davidson *et al.*, 2013), and increasing LREE/MREE (e.g. $[Nd/Dy]_n$) and LREE/HREE suggests breakdown of LREE-enriched minerals such as apatite or monazite (Fig. 8F), which are commonly consumed during anatexis (Yakymchuk, 2017). Decreasing $(Ce/Nd)_n$ during stage 1 (Fig. 8E) favors apatite (D_{Ce}/D_{Nd} = ~0.6; Sano *et al.*, 2002) over monazite (D_{Ce}/D_{Nd} = ~1; Stepanov *et al.*, 2012) and helps rule out other LREE-rich phases such as epidote and allanite. Another possibility is that ilmenite replaced titanite (D_{Ce}/D_{Nd} = ~0.3; Loader *et al.*, 2022) during prograde metamorphism. At ~700 MPa, ilmenite stabilizes at the expense of titanite at ~700 °C for most felsic rocks (Kohn, 2017).

Zircon crystallization during stage 1 is interpreted to have occurred in the source (forming a migmatite), prior to melt extraction, and records the earliest stages of anatexis. The zircon age population centered on ~58 Ma may represent the first significant melting–crystallization event in the source. The range of ages is interpreted to represent semi-continuous, small-volume, partial melting and crystallization that formed leucosomal bodies. Similar interpretations have been proposed for Himalayan leucogranites that have concordant U–Th–Pb accessory mineral dates and display a correlation between age and U concentration (e.g. Viskupic *et al.*, 2005; Lederer *et al.*, 2013; Cottle *et al.*, 2018; Xie *et al.*, 2018; Hopkinson *et al.*, 2020; Lin *et al.*, 2020; Chen *et al.*, 2021) analogous to that shown in Fig. 8A. These interpretations are supported by geochronological studies of Himalayan migmatites that demonstrate semi-continuous accessory mineral growth during partial melting and metamorphism (e.g. Imayama *et al.*, 2012; Rubatto *et al.*, 2013; Zhang *et al.*, 2017; Yang *et al.*, 2019; Kang *et al.*, 2020). Mass balance modeling of zircon in general suggests that primary zircon crystallization should be minimal during prograde metamorphism, but several studies document prograde, suprasolidus zircon growth, thought to occur primarily by dissolution–reprecipitation, Ostwald ripening, peritectic shielding, and open-system processes (Kelsey & Powell, 2011; Rubatto, 2017; Kohn & Kelly, 2018; Yakymchuk, 2023). Open-system processes, including localized injection of melt into migmatite during prograde metamorphism (e.g. Yakymchuk, 2023), are particularly appealing because it can explain increasing Pan Tak Granite $T_{Ti\text{-}zr}$ during stage 1. Zircon crystallization in a high-temperature, metamorphic environment is supported by zircon textures, including patchy textures and convoluted zoning (Fig. 6E, F). The patchy textures consist of bright CL (low-U)

recrystallized domains that replaced primary, dark CL (high-U) zircon interiors. These domains are consistent with fluid-assisted, coupled dissolution–reprecipitation reactions in high-T metamorphic environments that preferentially replaced self-irradiated, structurally damaged zircon with new crystalline zircon (Pidgeon *et al.*, 1998; Hoskin & Black, 2000; Rubatto & Gebauer, 2000; Schaltegger *et al.*, 2002; Geisler *et al.*, 2007; Vonlanthen *et al.*, 2012). Convoluted zoning (Fig. 6D, E) is common in high-T metamorphic rocks and predominantly results from solid-state recrystallization and diffusion of trace elements (Pidgeon *et al.*, 1998; Vavra *et al.*, 1999; Hoskin & Black, 2000; Corfu *et al.*, 2003; Kelly & Harley, 2005; Tichomirowa *et al.*, 2005; Harley *et al.*, 2007; Rubatto, 2017).

Stage 2 is characterized by a prominent age gap in zircon dates, observed from 53 to 51 Ma (Fig. 7B). Similar age gaps have been documented in studies of Himalayan leucogranites and have generally been interpreted to represent a period of significant melting and/or melt emplacement (Zeng *et al.*, 2015; Cottle *et al.*, 2018; Ding *et al.*, 2021; Ji *et al.*, 2022). Partial melting results in a hiatus in zircon crystallization and a switch to zircon dissolution in order to maintain Zr saturation as melt fraction increases (Kelsey & Powell, 2011; Kohn *et al.*, 2015; Yakymchuk *et al.*, 2017). We propose a similar explanation for the Pan Tak Granite age gap and suggest that this time interval records peak metamorphism and peak melt generation. There is textural evidence for zircon dissolution in the two-mica granite (e.g. Fig. 6H; right side of crystal) that preceded (re)crystallization of the high-U overgrowths. We also interpret the 53- to 51-Ma age gap to be the approximate time of melt extraction from the source and emplacement for the two-mica granite (Fig. 9). This interpretation, in which a paucity of dates represents the main melt extraction and emplacement event, is counterintuitive but may be a characteristic feature of anatectic leucogranites (Kohn *et al.*, 2015; Cottle *et al.*, 2018). Zircons previously crystallized during stage 1 are interpreted to have been mobilized and transported as antecrysts in the melt. Similar hypotheses have been proposed for Himalayan leucogranites that exhibit a range of ages (e.g. Langille *et al.*, 2012; Lederer *et al.*, 2013). The Pan Tak Granite age gap also defines an inflection point, or reversal, in geochemical–temporal trends that suggest a change from metamorphism and melt generation to crystallization and cooling in the third and final stage of the crystallization sequence (Fig. 8).

The third stage, from 51 to 42 Ma, is almost entirely defined by zircon crystallization in the leucogranite, although a few zircon U–Pb dates were obtained from high U (dark in CL images) overgrowths (i.e. rims) from the two-mica granite (Fig. 6G, H). Most of these overgrowths were too thin (few micrometers) to be measured by the methods employed (laser ablation spots of 20–40 μm on polished crystals), limiting the total number of analyses. These overgrowths are interpreted to represent new thermal- and/or fluid-mediated zircon (re)crystallization (e.g. Harley *et al.*, 2007; Rubatto *et al.*, 2009; Rubatto, 2017) that occurred during or after emplacement of the Pan Tak Granite (Fig. 9), potentially concurrent with zircon crystallization associated with the leucogranite (Fig. 9). *In situ* zircon recrystallization and the formation of high-U overgrowths are usually associated with metamorphic rocks but are also common in igneous rocks (e.g. Gaynor *et al.*, 2022) including in the Himalayan leucogranite belt where leucogranite dike swarms intrude two-mica granite (Liu *et al.*, 2014; Zeng *et al.*, 2015; Gao *et al.*, 2021; Gu *et al.*, 2022).

For the Pan Tak Granite, $T_{Ti\text{-}zr}$ decreases during the third stage, with the majority of calculated temperatures <700 °C (Fig. 8G) interpreted to represent cooling and crystallization. Several whole rock fractionation trends support leucogranite crystallization from a relatively cool, evolved melt: low Ba, low K/Rb, low Eu/Eu* (deeper Eu anomaly), low LREE, and high Rb/Sr (Fig. 4) (see section below). Zircon U/Th increases to 35–40 during the third stage (Fig. 8C). Zircon U/Th ratios ≥10 are commonly associated with metamorphic processes (e.g. Gehrels *et al.*, 2009), but here we interpret high U/Th to be related to crystallization from a highly fractionated melt, enriched in U (Kirkland *et al.*, 2015), and preferential and earlier crystallization of monazite (sequestering Th) compared to zircon (Yakymchuk *et al.*, 2018; Yakymchuk & Brown, 2019). Decreasing $(Nd/Dy)_n$ during stage 3 indicates crystallization of a LREE-enriched phase, and relatively constant $(Ce/Nd)_n$ suggests that this phase is more likely monazite than apatite (Fig. 8E, F). Decreasing zircon HREE and increasing $(Dy/Yb)_n$ during the third stage are interpreted to reflect garnet crystallization from melt rather than metamorphic garnet growth in the source region as temperature decreases (Fig. 8E, F). Increases in whole rock Dy/Yb for the most highly evolved samples (lowest MgO; Fig. 4G) also support garnet fractionation (e.g. Davidson *et al.*, 2013). Increasing zircon Hf with decreasing U–Pb age (Fig. 8B) and decreasing whole rock Zr/Hf with increasing SiO_2 (Fig. 4H) document zircon crystallization (e.g. Claiborne *et al.*, 2006). Apparent lack of inherited zircons in the leucogranite suggests that it crystallized primarily from residual melt (Fig. 9). Finally, the late-stage overgrowths (bright CL, low-U domain in Fig. 6D) that discordantly crosscut oscillatory zoning and spongy textures in zircons from the aplite dikes suggest a coupled dissolution–reprecipitation process mediated by aqueous fluids and/or melt that resulted in zircon (re)crystallization (Schaltegger *et al.*, 1999; Hoskin & Black, 2000; Rubatto & Gebauer, 2000; Geisler *et al.*, 2007; Vonlanthen *et al.*, 2012). Recrystallized zircon rims with similar textural relationships are common in high-grade metamorphic rocks and anatectic granites (Vavra *et al.*, 1996; Pidgeon *et al.*, 1998; Corfu *et al.*, 2003; Hoskin & Schaltegger, 2003; Tomaschek *et al.*, 2003; Harley *et al.*, 2007; Marsh & Stockli, 2015; Farina *et al.*, 2018).

Melt and differentiation mechanisms

The association of two-mica granite and tourmaline- or garnet-bearing leucogranite is common in anatectic provinces globally, including in the Himalayan leucogranite belt (Guo & Wilson, 2012). These two rock types have been interpreted as representing some combination of (1) different melt fractions produced during prograde heating (Visonà *et al.*, 2012; Gou *et al.*, 2016), (2) melting of different protoliths (Guillot & Le Fort, 1995), (3) different melting mechanisms (e.g. fluid-present vs fluid-absent melting; Inger & Harris, 1993; Gao *et al.*, 2017), and (4) residual melts formed by fractional crystallization (Scaillet *et al.*, 1990; Liu *et al.*, 2016). Field relations and geochemical and geochronological data from the Pan Tak Granite indicate the leucogranite formed from a highly fractionated, residual melt that differentiated from the magmas that produced the two-mica granite. The two-mica granite is interpreted to represent a frozen crystal, cumulate mush, and the leucogranite is interpreted to represent the residual, interstitial melt that was extracted from that mush. Similar interpretations for two-mica granite intruded by leucogranite have been proposed for parts of the Himalayan leucogranite belt (Liu *et al.*, 2019; Wu *et al.*, 2020).

Other explanations for the relationship between the two-mica granite and leucogranite can be ruled out. First, leucogranite intrudes two-mica granite, and zircon U–Pb data indicate that it crystallized after the two-mica granite. This is inconsistent with a hypothesis that the leucogranite represents a first-liquid,

minimum melt and that the two-mica granite was generated from greater degrees of partial melting at a higher temperature during prograde metamorphism (e.g. Visonà *et al.*, 2012). Second, initial crystallization of the two-mica granite argues against melting of different protoliths. Discrimination diagrams like Fe_2O_3 vs Na_2O/K_2O (Fig. 4C; Weinberg & Hasalová, 2015) could be used to infer melting of a biotite-rich protolith for the two-mica granite and a more muscovite-rich protolith for the leucogranite. However, higher-temperature melting of a more refractory protolith (e.g. biotite gneiss) is unlikely to occur prior to low-temperature melting of a more melt-fertile protolith (e.g. muscovite schist) (cf. Patiño-Douce & Harris, 1998). Geochemical and isotopic data also suggest that both the two-mica granite and leucogranite were chiefly derived from melting of the same (meta)igneous source rocks (Fig. 5). Decreasing Fe_2O_3 in Fig. 4C, from the two-mica granite toward the leucogranite, is interpreted to represent early and continued crystallization of biotite, the only major mafic phase present in the Pan Tak Granite, followed by crystallization of K-feldspar, quartz, and muscovite. Decreasing Na_2O/K_2O may also be caused by decreasing pressure of partial melting (Bartoli, 2021).

Several additional observations support fractional crystallization within the Pan Tak Granite. The Pan Tak leucogranite is strongly depleted in LREE compared to the two-mica granite (Fig. 4D), which is common in highly differentiated, very felsic magmas that have crystallized a LREE-rich phase such as monazite (Miller & Mittlefehldt, 1982). Some leucogranites exhibit a tetrad REE pattern (Fig. 4D), which is present in highly differentiated rocks and has been interpreted to indicate advanced fractionation and/or melt–fluid interaction, including crystallization from a residual aqueous fluid (McLennan, 1994; Irber, 1999; Stepanov *et al.*, 2012). The Pan Tak leucogranite has more negative Eu anomalies (lower Eu/Eu∗) than the two-mica granite (Fig. 8D), consistent with zircon Eu/Eu∗ trends, and supports fractionation related to feldspar crystallization (Holder *et al.*, 2020). Himalayan leucogranites are also commonly LREE depleted and have low Eu/Eu∗ relative to the two-mica granites that they intrude, including leucogranites from the Yardoi, Dala, Ramba, Malashan, and Peikucuo gneiss domes (Zeng *et al.*, 2011; Aikman *et al.*, 2012; Gao & Zeng, 2014; Liu *et al.*, 2014, 2019; Gao *et al.*, 2017; Wu *et al.*, 2020). High Rb/Sr and low K/Rb in the Pan Tak leucogranite, compared to the two-mica granite, suggest crystallization of K-feldspar (Fig. 4I). K/Rb ratios below chondritic values, particularly <150, have been interpreted to only arise from highly fractionated magmas (Dostal & Chatterjee, 2000; Blevin, 2004; Ballouard *et al.*, 2016). The Pan Tak two-mica granite has chondritic whole rock Zr/Hf ratios, but the leucogranite has subchondritic ratios (Fig. 4H), indicating zircon crystallization during differentiation (Linnen & Keppler, 2002; Claiborne *et al.*, 2006) and consistent with increasing zircon Hf concentrations through time (Fig. 8B) as Zr is preferentially depleted in the melt. Mineralogical and geochemical evidence also indicates late crystallization of garnet. The two-mica granite has whole rock Dy/Yb ratios similar to bulk continental crust, but the most evolved (lowest MgO) leucogranite samples show elevated Dy/Yb, consistent with the preferential removal of HREE from the melt by the crystallization of garnet (e.g. Davidson *et al.*, 2007) (Fig. 4G). Zircons from the Pan Tak leucogranite also show decreasing Yb and increasing $(Dy/Yb)_n$ concentrations through time, consistent with fractional crystallization of garnet and/or xenotime (Fig. 8E, F).

The Pan Tak Granite exhibits a sublinear, inverse relationship between Rb/Sr and Ba when plotted on a log–log plot (Fig. 4E). This trend can be interpreted to arise from muscovite dehydration melting or crystal fractionation of K-feldspar (Inger & Harris, 1993). Some studies of the Himalayan leucogranite belt have suggested it is more instructive to view this plot with Ba plotted on a linear scale (Gao *et al.*, 2017; Xie *et al.*, 2018). In this type of plot, three trends are apparent for the Pan Tak Granite: (1) a positive correlation between Rb/Sr and Ba at high Ba contents that is limited to the two-mica granite, (2) a negative correlation for intermediate Ba contents, and (3) an increase in Rb/Sr with no change in Ba for the lowest Ba contents that is limited to the leucogranite (Fig. 4F). A possible interpretation for these trends is progression from fluid-present (e.g. water-fluxed) muscovite melting to fluid-absent muscovite dehydration melting to fluid-absent biotite dehydration melting (Inger & Harris, 1993), which would suggest progressive increase in temperature in the source region. However, this interpretation is inconsistent with field observations, geochronology, and thermometric data showing that the relatively hot two-mica granite was intruded by the relatively cool leucogranite. Instead, we interpret the three trends in Fig. 4F to be related to fractionation of biotite, K-feldspar, and plagioclase. Crystal fractionation of these minerals produces geochemical trends similar to fluid-present muscovite melting and fluid-absent muscovite and biotite melting (Inger & Harris, 1993). Early biotite fractionation in the two-mica granite followed by feldspar fractionation in both phases is consistent with modal mineralogy, petrography, changes in whole rock Fe_2O_3, K/Rb, and Eu/Eu∗, and zircon Eu/Eu∗ trends. In addition, recent studies have suggested that LILE systematics (e.g. Inger & Harris, 1993) is an unreliable indicator of the fluid regime during anatexis (Schwindinger *et al.*, 2019; Bartoli, 2021).

Regional tectonic implications

One of major outstanding questions regarding the North American Cordilleran Anatectic Belt is what tectonic processes ultimately caused crustal melting (Chapman *et al.*, 2021). This problem is particularly acute for the southern US and northern Mexican Cordillera where migmatitic or high-grade metamorphic rocks associated with this melting event are not exposed. New data from the Pan Tak Granite provide some insight into this question. Unlike the northern Cordilleran Anatectic Belt (e.g. Thor-Odin, Valhalla; Gordon *et al.*, 2008), extension and exhumation in the Coyote Mountains metamorphic core complex (29–24 Ma; Gottardi *et al.*, 2020) are significantly younger than the Pan Tak Granite, so decompression melting related to extension is unlikely. However, the region experienced shortening during the Laramide orogeny (e.g. Clinkscales & Lawton, 2018), contemporaneous with crystallization of the Pan Tak Granite, and decompression associated with exhumation during contractional deformation remains a possibility. Syn-convergent Late Cretaceous to Paleogene extension has been documented regionally (Wells & Hoisch, 2008; Wong *et al.*, 2023) and could help explain anatexis.

There is no evidence for increased mantle heat flow caused by upwelling asthenospheric mantle (e.g. delamination, plume, extension) in southern Arizona during the Laramide orogeny. The region is thought to have had relatively thick crust (Chapman *et al.*, 2020) and be underlain by the shallowly subducting Farallon plate that may have cooled the upper plate (Dumitru *et al.*, 1991; Liu & Currie, 2016). The modern mantle lithosphere and lower crust appear to be intact (Kumar *et al.*, 2012), and age-equivalent mantle-derived mafic igneous rocks are generally absent.

The geochemistry of the Pan Tak Granite is inconsistent with water-excess melting, where free water remains in the protolith above the solidus and anatectic melts are water saturated (Fig. 4). However, water-deficient melting, where partial melting

consumes all free water at the solidus and water-undersaturated melts are produced (Nabelek, 2019; Schwindinger *et al.*, 2019; Chapman *et al.*, 2021), is plausible and perhaps likely given the estimates for magma temperatures <700 °C at the onset of crustal melting (early stage 1). In general, it is difficult to distinguish between fluid-absent dehydration melting and fluid-deficient melting using geochemical data alone (Weinberg & Hasalová, 2015; Bartoli, 2021). External fluids, including water, could have been supplied from dehydration reactions in the Farallon slab or exsolved from intrusive rocks associated with the Laramide continental arc. The addition of fluids has been proposed to help explain the large volumes of supracrustal derived melts exposed in the North American Cordilleran Belt and by inference, large melt volumes produced within the crust (Chapman *et al.*, 2021). Based on the trend of increasing $T_{Ti\text{-}zr}$ during stage 1 for the Pan Tak two-mica granite (Fig. 8G), we propose that the maximum temperatures reached during the stage 2 age gap were ≥850 °C, when the largest melt volumes were produced, and zircon was being dissolved rather than crystallized (Fig. 9). These maximum temperature estimates are consistent with biotite dehydration melting, may help explain the presence of biotite in the two-mica granite, and obviate the need for external fluids to produce the large melt volumes observed. If zircon dissolution is common during peak metamorphism and melt generation in other parts of the North American Cordilleran Belt, then maximum temperature estimates based on zircon thermometers could systematically underestimate magma temperature because zircon is not crystallizing during these peak conditions.

In any scenario, added water by itself could not have caused crustal melting because the Pan Tak Granite shows a protracted prograde metamorphic history from 62 to 53 Ma. Adding water to an already hot lower crust should produce melts with similar or decreasing crystallization temperatures. The protracted prograde history also leads us to disfavor the possibility of decompression melting during exhumation associated with contractional deformation as a primary cause of melting as this model predicts cooling or near isothermal conditions (e.g. Whitney *et al.*, 2004). We suggest that (1) radiogenic heating and relaxation of isotherms following crustal thickening (Haxel *et al.*, 1984), (2) heat transfer related to the Laramide arc, and (3) shear heating associated with deformation are the most likely heat sources driving crustal melting in the Coyote Mountains. During the mid-Cretaceous, southern Arizona was close to sea level and marine carbonates were deposited in the Bisbee Basin (Dickinson & Lawton, 2001), suggesting the crust had normal thickness or was relatively thin. By Late Cretaceous time, however, the region was in the throes of the Laramide orogeny and geochemical data suggest that the crust had thickened to approximately 55–60 km and formed an orogenic plateau called the Arizonaplano (Chapman *et al.*, 2020; Jepson *et al.*, 2022). There is an apparent lack of significant crustal shortening in southern Arizona during the Sevier-Laramide orogeny; however, thickening may have been caused by magmatic additions to the crust rather than tectonic shortening alone (Erdman *et al.*, 2016; Chapman *et al.*, 2020). There is a strong association between orogenic plateaus and anatectic belts globally, with the Tibetan Plateau being the archetype, because crustal thickening may lead to an increase in the concentration of radiogenic elements within the crust and relaxation of isotherms after thickening increases temperatures in the deep crust (e.g. England & Thompson, 1984). A potential problem with invoking radiogenic decay and thermal relaxation as the cause of heating is that numerical models suggest that maximum temperatures are achieved only after significant incubation times, ~20 Myr as a minimum and in some cases >50 Myr after crustal thickening begins (Vanderhaeghe *et al.*, 2003; Jamieson & Beaumont, 2013). Shorter incubation times are possible, especially if fluids helped to advect heat, but there may have been too little time between crustal thickening and the onset of anatexis in southern Arizona. Regardless, crustal thickening related to the Sevier-Laramide orogeny is likely to have played a major role in crustal melting (Patiño-Douce *et al.*, 1990). The prograde metamorphic history for the Pan Tak Granite suggests that significant exhumation and cooling did not occur during the Laramide orogeny, at least locally. This supports the hypothesis that the region was characterized by a low-relief orogenic plateau experiencing limited erosion (Chapman *et al.*, 2020), consistent with the widespread presence of unmetamorphosed Paleozoic to Mesozoic sedimentary and volcanic rocks.

In south-central Arizona, Laramide continental arc rocks are generally 75–55 Ma and partially overlap in age with the Pan Tak Granite and the onset of crustal melting (Chapman *et al.*, 2018; Seedorff *et al.*, 2019). Laramide arc rocks are not exposed in the Coyote Mountains or Baboquivari Mountains but can be found in neighboring mountain ranges, including the 65- to 58-Ma Ruby Star Granodiorite in the Sierrita Mountains (Fig. 1) (Johnson *et al.*, 2003). Several studies have demonstrated that the repeated injection of mantle-derived magmas (e.g. basaltic dikes) into the lower crust in continental arcs increases background temperatures, which can cause 'pure' crustal melting of country rocks (Dufek & Bergantz, 2005; Annen *et al.*, 2006). However, these melts are thought to chiefly homogenize with mantle-derived magmas in the deep crust to produce the intermediate magmas that dominate continental arcs (Hildreth & Moorbath, 1988). The products of 'pure' crustal melting observed in continental arc batholiths (e.g. peraluminous leucogranites) tend to be low volume, surrounded by and dwarfed by intermediate metaluminous arc rocks, and form either early or late in intrusive suites (e.g. Barnes *et al.*, 2021; Quintero *et al.*, 2021). The Pan Tak Granite differs from these examples of crustal melting in continental arcs and was not generated from mantle-derived magmas intruded into the lower crust. However, magmatic activity related to the Laramide arc is likely to have transferred heat and/or fluids into the surrounding crust and contributed to overall crustal heating as suggested by Haxel *et al.* (1984).

Deformation may also have contributed to crustal heating. Shear heating in the lower to mid-crust has been proposed to cause crustal melting in some collisional orogens, including the Himalayan-Tibet orogen (Molnar & England, 1990; Harrison *et al.*, 1998; Nabelek & Liu, 1999). Other studies, however, have questioned whether shear heating within the crust produces enough heat to cause melting and suggest that heating is short-lived (<5 Myr) and localized (Platt, 2015). Contractional deformation in southern Arizona during the Laramide orogeny is thought to have been characterized chiefly by high-angle reverse faulting, resulting in basement-cored uplifts (Favorito & Seedorff, 2022), which may not be as prone to shear heating as the large, mid-crustal, subhorizontal shear zones in the Himalaya and other collisional orogens. Another possibility is that viscous heating occurred in the upper lithospheric mantle during deformation and increased heat flow into the base of the crust (e.g. Burg & Gerya, 2005; Hartz & Podladchikov, 2008). Some numerical models for shallow subduction of the Farallon plate beneath North America predict shearing within the mantle lithosphere and high positive deviatoric stresses in the uppermost mantle that could facilitate heating (Liu & Currie, 2016; Axen *et al.*, 2018).

CONCLUSIONS

We have emphasized the similarities between the Himalayan leucogranite belt and the southern North American Cordilleran Anatectic Belt, as represented by the Pan Tak Granite. Melt processes and differentiation mechanisms interpreted for the Pan Tak Granite are also common in other major anatectic provinces including the Caledonides, Variscan/Hercynian, Alpine, Araçuaí, and North Qiadam orogenic systems (Bea *et al.*, 1994; Villaseca *et al.*, 1998; Pedrosa-Soares *et al.*, 2001; Burri *et al.*, 2005; Gordon *et al.*, 2013; Marsh & Stockli, 2015; Laurent *et al.*, 2017; Kirkland *et al.*, 2018; Yu *et al.*, 2019). However, the Himalayan leucogranite belt is the most well-studied anatectic province globally (e.g. Guo & Wilson, 2012), is at the forefront of debates surrounding the petrogenesis of leucogranites and crustal melting mechanisms (e.g. Visonà & Lombardo, 2002), and is the basis for many fundamental geodynamic models linking anatexis to tectonics (e.g. England & Thompson, 1984; Molnar *et al.*, 1993; Beaumont *et al.*, 2004). The Himalayan-Tibetan orogen is also the archetype for orogens constructed by continental collision and highlights how remarkable it is to find a major anatectic province in a Cordilleran orogenic system. For example, all the major anatectic provinces listed above formed in continental collisional orogens. Because of the lack of migmatite and high-grade metamorphic rocks related to the Sevier-Laramide orogeny in the southern US and northern Mexican Cordillera, the metamorphic history of this region has remained relatively unknown. Our new data from the Pan Tak Granite represent some of the first constraints on metamorphism and the conditions of anatexis in the region and demonstrates how profound the orogenic and thermal event was, particularly for the deep crust.

The Pan Tak Granite is a plutonic body of two-mica ± garnet granite intruded by muscovite ± garnet leucogranite dikes. The two-mica granite represents a frozen crystal (cumulate) mush, and the leucogranite dikes represent a residual melt that formed by fractional crystallization from the two-mica granite magma. The Pan Tak Granite exhibits several characteristics of highly fractioned granites including subchondritic Zr/Hf and K/Rb, LREE and Eu depletion, and zircon Hf and U enrichment. The Pan Tak Granite formed by partial melting of pre-existing (meta)igneous rocks including Jurassic and Proterozoic granitoids. The Pan Tak Granite exhibits a wide range of zircon U–Pb ages (62–42 Ma) that record a three-stage crystallization sequence. The first stage, from approximately 62–53 Ma, documents initiation of crustal melting and prograde metamorphism. $T_{Ti\text{-}zr}$ increases from 650 to 850 °C, and the increasing zircon REE concentrations are interpreted to record prograde breakdown of apatite and/or replacement of titanite by ilmenite. During this interval, zircons are interpreted to have crystallized from discontinuous, small-volume partial melts in a migmatite (i.e. leucosomes) in the deep crust. Melt volume and melt connectivity increased during stage 1 metamorphism, eventually leading to melt extraction, ascent, and emplacement into the mid-crust during stage 2. Zircons in the two-mica granite that crystallized during stage 1 are antecrysts transported as a crystal cargo during melt extraction.

Stage 2, approximately 53–51 Ma, records peak metamorphic conditions ($T > 850$ °C). This stage is characterized by a zircon U–Pb age gap caused by a shift to zircon dissolution as the melt fraction increased and the melt became undersaturated in Zr. This dissolution event is texturally recorded in zircons from the two-mica granite and preserved by the formation of high-U overgrowths (rims), which crystallized from a more strongly fractionated residual melt during stage 3. Stage 3, approximately 51–42 Ma, records cooling ($T_{Ti\text{-}zr} < 700$ °C) and crystallization of the Pan Tak Granite after emplacement. Leucogranite dikes formed during this period and crystallized from a relatively pure, crystal poor, residual melt. Zircons from the leucogranite lack inherited xenocrystic components and have relatively high U/Th, predominantly owing to crystallization of monazite, which also caused whole rock LREE depletion. The residual melt was water rich, and the youngest leucogranite dikes are pegmatitic. Aqueous fluids associated with intrusion and crystallization of the leucogranite dikes caused *in situ* alteration of mineral phases, including diffusion–reaction processes that produced the microporous, spongy texture in zircons. Zircon alteration was aided by high U concentrations and consequent radiation damage.

The relatively low magma temperature estimates (650–700 °C) at the onset of crustal melting during stage 1 suggest some free water may have been present, but the geochemistry of the Pan Tak Granite is inconsistent with water-saturated melting. Anatexis is interpreted to have started as water-deficient melting at lower temperatures and evolved into water-absent, dehydration melting at higher temperatures, by the end of stage 1. Free water may have been sourced from the subducting Farallon slab or exsolved from older Laramide arc rocks. Metamorphism and anatexis in the southern US Cordillera was not a short, punctuated event but a protracted process that affected the deep crust for >10 Myr. The most probable causes of protracted crustal heating are radiogenic heating and relaxation of isotherms associated with crustal thickening, heat transfer related to the Laramide arc, and shear and viscous heating related to deformation of the deep lithosphere. The Pan Tak Granite is an analog for crustal melting and anatectic processes occurring in the modern Tibetan Plateau and Altiplano. Low-relief orogenic plateaus characterized by thick crust, high heat flow, and low erosion may be essential for the formation of anatectic belts in Cordilleran orogens, including the Arizonaplano in the southern US and northern Mexican Cordillera.

Data Availability

The geochemical, isotopic, and geochronological data in this article are available in the article and in its online supplementary material.

Supplementary Data

Supplementary data are available at Journal of Petrology online.

Acknowledgements

The manuscript was improved by thoughtful discussion with Gary Axen and careful reviews from Omar Bartoli, Frederico Farina, Christopher Spencer, and an anonymous reviewer. Chapman acknowledges support from US National Science Foundation grant EAR-1928312. Ducea acknowledges grant C1.2.PFE-CDI.2021-587/contract no. 41PFE/30.12.2021 from the Romanian Ministry of Research, Innovation and Digitization (MCID).

References

Aikman, A. B., Harrison, T. M. & Hermann, J. (2012). The origin of Eo-and Neo-himalayan granitoids, Eastern Tibet. *Journal of Asian Earth Sciences* **58**, 143–157. https://doi.org/10.1016/j.jseaes.2012.05.018.

Anderson, J. L. & Bender, E. E. (1989). Nature and origin of Proterozoic A-type granitic magmatism in the southwestern United States of America. *Lithos* **23**, 19–52. https://doi.org/10.1016/0024-4937(89)90021-2.

Anderson, J. L. & Morrison, J. (2005). Ilmenite, magnetite, and peraluminous Mesoproterozoic anorogenic granites of Laurentia and Baltica. *Lithos* **80**, 45–60. https://doi.org/10.1016/j.lithos.2004.05.008.

Annen, C., Blundy, J. D. & Sparks, R. S. J. (2006). The genesis of intermediate and silicic magmas in deep crustal hot zones. *Journal of Petrology* **47**, 505–539. https://doi.org/10.1093/petrology/egi084.

Axen, G. J., van Wijk, J. W. & Currie, C. A. (2018). Basal continental mantle lithosphere displaced by flat-slab subduction. *Nature Geoscience* **11**, 961–964. https://doi.org/10.1038/s41561-018-0263-9.

Ballouard, C., Poujol, M., Boulvais, P., Branquet, Y., Tartese, R. & Vigneresse, J. L. (2016). Nb-Ta fractionation in peraluminous granites: a marker of the magmatic-hydrothermal transition. *Geology* **44**, 231–234. https://doi.org/10.1130/G37475.1.

Barnes, C. G., Coint, N., Barnes, M. A., Chamberlain, K. R., Cottle, J. M., Rämö, O. T., Strickland, A. & Valley, J. W. (2021). Open-system evolution of a crustal-scale magma column, Klamath Mountains, California. *Journal of Petrology* **62**, egab065. https://doi.org/10.1093/petrology/egab065.

Barovich, K. M. (1991) *Behavior of Lutetium–Hafnium, Samarium–Neodymium and Rubidium–Strontium Isotopic Systems during Processes Affecting Continental Crust*. Ph.D. thesis,. Tucson: University of Arizona.

Bartoli, O. (2021). Granite geochemistry is not diagnostic of the role of water in the source. *Earth and Planetary Science Letters* **564**, 116927. https://doi.org/10.1016/j.epsl.2021.116927.

Bartoli, O. & Carvalho, B. B. (2021). Anatectic granites in their source region: a comparison between experiments, thermodynamic modelling and nanogranitoids. *Lithos* **402-403**, 106046. https://doi.org/10.1016/j.lithos.2021.106046.

Bea, F., Pereira, M. D., Corretgé, L. G. & Fershtater, G. B. (1994). Differentiation of strongly peraluminous, perphosphorus granites: the Pedrobernardo pluton, Central Spain. *Geochimica et Cosmochimica Acta* **58**, 2609–2627. https://doi.org/10.1016/0016-7037(94)90132-5.

Beaumont, C., Jamieson, R. A., Nguyen, M. H. & Medvedev, S. (2004). Crustal channel flows: 1. Numerical models with applications to the tectonics of the Himalayan-Tibetan orogen. *Journal of Geophysical Research: Solid Earth* **109**, B06406.

Blevin, P. L. (2004). Redox and compositional parameters for interpreting the granitoid metallogeny of eastern Australia: implications for gold-rich ore systems. *Resource Geology* **54**, 241–252. https://doi.org/10.1111/j.1751-3928.2004.tb00205.x.

Bright, R. M., Amato, J. M., Denyszyn, S. W. & Ernst, R. E. (2014). U-Pb geochronology of 1.1 Ga diabase in the southwestern United States: testing models for the origin of a post-Grenville large igneous province. *Lithosphere* **6**, 135–156. https://doi.org/10.1130/L335.1.

Budzyń, B., Sláma, J., Kozub-Budzyń, G. A., Konečný, P., Holický, I., Rzepa, G. & Jastrzębski, M. (2018). Constraints on the timing of multiple thermal events and re-equilibration recorded by high-U zircon and xenotime: case study of pegmatite from Piława Górna (Góry Sowie block, SW Poland). *Lithos* **310-311**, 65–85. https://doi.org/10.1016/j.lithos.2018.03.021.

Burg, J. P. & Gerya, T. V. (2005). The role of viscous heating in Barrovian metamorphism of collisional orogens: thermomechanical models and application to the Lepontine Dome in the Central Alps. *Journal of Metamorphic Geology* **23**, 75–95. https://doi.org/10.1111/j.1525-1314.2005.00563.x.

Burri, T., Berger, A. & Engi, M. (2005). Tertiary migmatites in the Central Alps: regional distribution, field relations, conditions of formation, and tectonic implications. *Swiss Bulletin of Mineralogy and Petrology* **85**, 215–232.

Busby, C. J. & Centeno-García, E. (2022). The "Nazas Arc" is a continental rift province: implications for Mesozoic tectonic reconstructions of the southwest Cordillera, US and Mexico. *Geosphere* **18**, 647–669. https://doi.org/10.1130/GES02443.1.

Chamberlain, K. J., Wilson, C. J., Wooden, J. L., Charlier, B. L. A. & Ireland, T. R. (2014). New perspectives on the Bishop Tuff from zircon textures, ages and trace elements. *Journal of Petrology* **55**, 395–426. https://doi.org/10.1093/petrology/egt072.

Chapman, J. B., Dafov, M. N., Gehrels, G., Ducea, M. N., Valley, J. W. & Ishida, A. (2018). Lithospheric architecture and tectonic evolution of the southwestern U.S. Cordillera: constraints from zircon Hf and O isotopic data. *GSA Bulletin* **130**, 2031–2046. https://doi.org/10.1130/B31937.1.

Chapman, J. B., Greig, R. & Haxel, G. B. (2020). Geochemical evidence for an orogenic plateau in the southern U.S. and northern Mexican Cordillera during the Laramide orogeny. *Geology* **48**, 164–168. https://doi.org/10.1130/G47117.1.

Chapman, J. B., Runyon, S. E., Shields, J. E., Lawler, B. L., Pridmore, C. J., Scoggin, S. H., Swaim, N. T., Trzinski, A. E., Wiley, H. N., Barth, A. P. & Haxel., G.B. (2021). The North American Cordilleran Anatectic Belt. *Earth-Science Reviews* **215**, 103576. https://doi.org/10.1016/j.earscirev.2021.103576.

Chen, X., Zhang, G., Gao, R., Zhang, D. & Yang, B. (2021). Petrogenesis of highly fractionated leucogranite in the Himalayas: the Early Miocene Cuonadong example. *Geological Journal* **56**, 3791–3807. https://doi.org/10.1002/gj.4126.

Claiborne, L. L., Miller, C. F., Walker, B. A., Wooden, J. L., Mazdab, F. K. & Bea, F. (2006). Tracking magmatic processes through Zr/Hf ratios in rocks and Hf and Ti zoning in zircons: an example from the Spirit Mountain batholith, Nevada. *Mineralogical Magazine* **70**, 517–543. https://doi.org/10.1180/0026461067050348.

Clinkscales, C. A. & Lawton, T. F. (2018). Mesozoic–Paleogene structural evolution of the southern US Cordillera as revealed in the Little and Big Hatchet Mountains, southwest New Mexico, USA. *Geosphere* **14**, 162–186. https://doi.org/10.1130/GES01539.1.

Corfu, F., Hanchar, J. M., Hoskin, P. W. & Kinny, P. (2003). Atlas of zircon textures. *Reviews in Mineralogy and Geochemistry* **53**, 469–500. https://doi.org/10.2113/0530469.

Cottle, J. M., Larson, K. P. & Yakymchuk, C. (2018). Contrasting accessory mineral behavior in minimum-temperature melts: empirical constraints from the Himalayan metamorphic core. *Lithos* **312-313**, 57–71. https://doi.org/10.1016/j.lithos.2018.05.003.

Curry, A., Gaynor, S. P., Davies, J. H. F. L., Ovtcharova, M., Simpson, G. & Caricchi, L. (2021). Timescales and thermal evolution of large silicic magma reservoirs during an ignimbrite flare-up: perspectives from zircon. *Contributions to Mineralogy and Petrology* **176**, 1–27. https://doi.org/10.1007/s00410-021-01862-w.

Davidson, J., Turner, S. & Plank, T. (2013). Dy/Dy∗: variations arising from mantle sources and petrogenetic processes. *Journal of Petrology* **54**, 525–537. https://doi.org/10.1093/petrology/egs076.

Davis, G. H., Spencer, J. E. & Gehrels, G. E. (2019). Field-trip guide to the Catalina–Rincon metamorphic core complex, Tucson. Arizona: geologic excursions in southwestern North America. *Geological Society of America Field Guide* **55**.

Delph, J. R., Ward, K. M., Zandt, G., Ducea, M. N. & Beck, S. L. (2017). Imaging a magma plumbing system from MASH zone to magma reservoir. *Earth and Planetary Science Letters* **457**, 313–324. https://doi.org/10.1016/j.epsl.2016.10.008.

Dickinson, W. R. & Lawton, T. F. (2001). Tectonic setting and sandstone petrofacies of the Bisbee basin (USA–Mexico). *Journal of South American Earth Sciences* **14**, 475–504. https://doi.org/10.1016/S0895-9811(01)00046-3.

Ding, H., Zhang, Z., Kohn, M. J. & Gou, Z. (2021). Timescales of partial melting and melt crystallization in the eastern Himalayan orogen: insights from zircon petrochronology. *Geochemistry, Geophysics, Geosystems* **22**, e2020GC009539. https://doi.org/10.1029/2020GC009539.

Dostal, J. & Chatterjee, A. K. (2000). Contrasting behaviour of Nb/Ta and Zr/Hf ratios in a peraluminous granitic pluton (Nova Scotia, Canada). *Chemical Geology* **163**, 207–218. https://doi.org/10.1016/S0009-2541(99)00113-8.

Ducea, M. N., Seclaman, A. C., Murray, K. E., Jianu, D. & Schoenbohm, L. M. (2013). Mantle-drip magmatism beneath the Altiplano-Puna plateau, central Andes. *Geology* **41**, 915–918. https://doi.org/10.1130/G34509.1.

Ducea, M. N., Triantafyllou, A. & Krcmaric, J. (2020). New timing and depth constraints for the Catalina metamorphic core complex, southeast Arizona. *Tectonics* **39**, e2020TC006383. https://doi.org/10.1029/2020TC006383.

Dufek, J. & Bergantz, G. W. (2005). Lower crustal magma genesis and preservation: a stochastic framework for the evaluation of basalt–crust interaction. *Journal of Petrology* **46**, 2167–2195. https://doi.org/10.1093/petrology/egi049.

Dumitru, T. A., Gans, P. B., Foster, D. A. & Miller, E. L. (1991). Refrigeration of the western Cordilleran lithosphere during Laramide shallow-angle subduction. *Geology* **19**, 1145–1148. https://doi.org/10.1130/0091-7613(1991)019<1145:ROTWCL>2.3.CO;2.

England, P. C. & Thompson, A. B. (1984). Pressure—temperature—time paths of regional metamorphism I. Heat transfer during the evolution of regions of thickened continental crust. *Journal of Petrology* **25**, 894–928. https://doi.org/10.1093/petrology/25.4.894.

England, P., Le Fort, P., Molnar, P. & Pecher, A. (1992). Heat sources for tertiary metamorphism and anatexis in the Annapurna-Manaslu region central Nepal. *Journal of Geophysical Research* **97**, 2107–2128. https://doi.org/10.1029/91JB02272.

Erdman, M. E., Lee, C. T. A., Levander, A. & Jiang, H. (2016). Role of arc magmatism and lower crustal foundering in controlling elevation history of the Nevadaplano and Colorado Plateau: a case study of pyroxenitic lower crust from central Arizona, USA. *Earth and Planetary Science Letters* **439**, 48–57. https://doi.org/10.1016/j.epsl.2016.01.032.

Ewing, R. C., Meldrum, A., Wang, L. M., Weber, W. J. & Corrales, L. R. (2003). Radiation effects in zircon. *Reviews in Mineralogy and Geochemistry* **53**, 387–425. https://doi.org/10.2113/0530387.

Farina, F., Dini, A., Davies, J. H., Ovtcharova, M., Greber, N. D., Bouvier, A. S., Baumgartner, L., Ulianov, A. & Schaltegger, U. (2018). Zircon petrochronology reveals the timescale and mechanism of anatectic magma formation. *Earth and Planetary Science Letters* **495**, 213–223. https://doi.org/10.1016/j.epsl.2018.05.021.

Farmer, G. L. & Depaolo, D. J. (1984). Origin of Mesozoic and tertiary granite in the western United States and implications for pre-Mesozoic crustal structure: 2. Nd and Sr isotopic studies of unmineralized and Cu-and Mo-mineralized granite in the Precambrian Craton. *Journal of Geophysical Research: Solid Earth* **89**, 10141–10160. https://doi.org/10.1029/JB089iB12p10141.

Favorito, D. A. & Seedorff, E. (2022). Laramide structure of southeastern Arizona: role of basement-cored uplifts in shallow-angle subduction. *Geological Society of America Bulletin* **134**, 989–1017. https://doi.org/10.1130/B35894.1.

Ferry, J. M. & Watson, E. B. (2007). New thermodynamic models and revised calibrations for the Ti-in-zircon and Zr-in-rutile thermometers. *Contributions to Mineralogy and Petrology* **154**, 429–437. https://doi.org/10.1007/s00410-007-0201-0.

Finch, M., Hasalová, P., Weinberg, R. F. & Fanning, C. M. (2014). Switch from thrusting to normal shearing in the Zanskar shear zone, NW Himalaya: implications for channel flow. *Geological Society of America Bulletin* **126**, 892–924. https://doi.org/10.1130/B30817.1.

Fornash, K. F., Patchett, P. J., Gehrels, G. E. & Spencer, J. E. (2013). Evolution of granitoids in the Catalina metamorphic core complex, southeastern Arizona: U–Pb, Nd, and Hf isotopic constraints. *Contributions to Mineralogy and Petrology* **165**, 1295–1310. https://doi.org/10.1007/s00410-013-0859-4.

Gao, L. E. & Zeng, L. S. (2014). Fluxed melting of metapelite and the formation of Miocene high-CaO two-mica granites in the Malashan gneiss dome, southern Tibet. *Geochimica et Cosmochimica Acta* **130**, 136–155. https://doi.org/10.1016/j.gca.2014.01.003.

Gao, L. E., Zeng, L. S. & Asimow, P. D. (2017). Contrasting geochemical signatures of fluid absent versus fluid-fluxed melting of muscovite in metasedimentary sources: the Himalayan leucogranites. *Geology* **45**, 39–42. https://doi.org/10.1130/G38336.1.

Gao, L. E., Zeng, L., Zhao, L., Hou, K., Guo, C., Gao, J. & Wang, Y. (2021). Geochemical behavior of rare metals and high field strength elements during granitic magma differentiation: a record from the Borong and Malashan Gneiss Domes, Tethyan Himalaya, southern Tibet. *Lithos* **398-399**, 106344. https://doi.org/10.1016/j.lithos.2021.106344.

Gaynor, S. P., Ruiz, M. & Schaltegger, U. (2022). The importance of high precision in the evaluation of U-Pb zircon age spectra. *Chemical Geology* **603**, 120913. https://doi.org/10.1016/j.chemgeo.2022.120913.

Gehrels, G. (2012) Detrital zircon U-Pb geochronology: current methods and new opportunities. In: Busby C. & Azor A. (eds) *Tectonics of Sedimentary Basins: Recent Advances*. Oxford: Wiley-Blackwell, pp. 45–62.

Gehrels, G., Rusmore, M., Woodsworth, G., Crawford, M., Andronicos, C., Hollister, L., Patchett, J., Ducea, M., Butler, R., Klepeis, K., Davidson, C., Friedman, R., Haggart, J., Mahoney, B., Crawford, W., Pearson, D. & Girardi, J. (2009). U-Th-Pb geochronology of the Coast Mountains batholith in north-coastal British Columbia: constraints on age and tectonic evolution. *Geological Society of America Bulletin* **121**, 1341–1361. https://doi.org/10.1130/B26404.1.

Geisler, T., Schaltegger, U. & Tomaschek, F. (2007). Re-equilibration of zircon in aqueous fluids and melts. *Elements* **3**, 43–50. https://doi.org/10.2113/gselements.3.1.43.

Goodwin, L. B. & Haxel, G. B. (1990). Structural evolution of the Southern Baboquivari Mountains, south-central Arizona and north-central Sonora. *Tectonics* **9**, 1077–1095. https://doi.org/10.1029/TC009i005p01077.

Gordon, S. M., Whitney, D. L., Teyssier, C., Grove, M. & Dunlap, W. J. (2008). Timescales of migmatization, melt crystallization, and cooling in a Cordilleran gneiss dome: Valhalla complex, southeastern British Columbia. *Tectonics* **27**, TC4010. https://doi.org/10.1029/2007TC002103.

Gordon, S. M., Whitney, D. L., Teyssier, C. & Fossen, H. (2013). U–Pb dates and trace-element geochemistry of zircon from migmatite, Western Gneiss Region, Norway: significance for history of partial melting in continental subduction. *Lithos* **170-171**, 35–53. https://doi.org/10.1016/j.lithos.2013.02.003.

Gottardi, R., McAleer, R., Casale, G., Borel, M., Iriondo, A. & Jepson, G. (2020). Exhumation of the Coyote Mountains metamorphic core complex (Arizona): implications for orogenic

collapse of the southern North American Cordillera. *Tectonics* **39**, e2019TC006050. https://doi.org/10.1029/2019TC006050.

Gou, Z., Zhang, Z., Dong, X., Xiang, H., Ding, H., Tian, Z. & Lei, H. (2016). Petrogenesis and tectonic implications of the Yadong leucogranites, southern Himalaya. *Lithos* **256-257**, 300–310. https://doi.org/10.1016/j.lithos.2016.04.009.

Gu, D., Zhang, J., Lin, C., Fan, Y., Feng, L., Zheng, J. & Liu, S. (2022). Anatexis and resultant magmatism of the Ama Drime Massif: implications for Himalayan mid-Miocene tectonic regime transition. *Lithos* **424-425**, 106773. https://doi.org/10.1016/j.lithos.2022.106773.

Gualda, G. A., Ghiorso, M. S., Lemons, R. V. & Carley, T. L. (2012). Rhyolite-MELTS: a modified calibration of MELTS optimized for silica-rich, fluid-bearing magmatic systems. *Journal of Petrology* **53**, 875–890. https://doi.org/10.1093/petrology/egr080.

Guillot, S. & Le Fort, P. (1995). Geochemical constraints on the bimodal origin of High Himalayan leucogranites. *Lithos* **35**, 221–234. https://doi.org/10.1016/0024-4937(94)00052-4.

Guo, Z. & Wilson, M. (2012). The Himalayan leucogranites: constraints on the nature of their crustal source region and geodynamic setting. *Gondwana Research* **22**, 360–376. https://doi.org/10.1016/j.gr.2011.07.027.

Harley, S. L., Kelly, N. M. & Möller, A. (2007). Zircon behaviour and the thermal histories of mountain chains. *Elements* **3**, 25–30. https://doi.org/10.2113/gselements.3.1.25.

Harris, N. & Massey, J. (1994). Decompression and anatexis of Himalayan metapelites. *Tectonics* **13**, 1537–1546. https://doi.org/10.1029/94TC01611.

Harrison, T. M., Grove, M., Lovera, O. M. & Catlos, E. J. (1998). A model for the origin of Himalayan anatexis and inverted metamorphism. *Journal of Geophysical Research: Solid Earth* **103**, 27017–27032. https://doi.org/10.1029/98JB02468.

Hartz, E. H. & Podladchikov, Y. Y. (2008). Toasting the jelly sandwich: the effect of shear heating on lithospheric geotherms and strength. *Geology* **36**, 331–334. https://doi.org/10.1130/G24424A.1.

Haxel, G. B., Tosdal, R. M., May, D. J. & Wright, J. E. (1984). Latest Cretaceous and early Tertiary orogenesis in south-central Arizona: thrust faulting, regional metamorphism, and granitic plutonism. *Geological Society of America Bulletin* **95**, 631–653. https://doi.org/10.1130/0016-7606(1984)95<631:LCAETO>2.0.CO;2.

Haxel, G. B., May, D. J., Anderson, T. H., Tosdal, R. M., Wright, J. E., Spencer, J. E. & Titley, S. R. (2008). Geology and geochemistry of Jurassic plutonic rocks, Baboquivari Mountains, south-central Arizona. Ores and orogenesis: Circum-Pacific tectonics, geologic evolution, and ore deposits. *Arizona Geological Society Digest* **22**, 497–515.

Hildreth, W. & Moorbath, S. (1988). Crustal contributions to arc magmatism in the Andes of central Chile. *Contributions to Mineralogy and Petrology* **98**, 455–489. https://doi.org/10.1007/BF00372365.

Hodges, K. V. (1998). The thermodynamics of Himalayan orogenesis. *Geological Society, London, Special Publication* **138**, 7–22. https://doi.org/10.1144/GSL.SP.1996.138.01.02.

Holder, R. M., Yakymchuk, C. & Viete, D. R. (2020). Accessory mineral Eu anomalies in suprasolidus rocks: beyond feldspar. *Geochemistry, Geophysics, Geosystems* **21**, e2020GC009052. https://doi.org/10.1029/2020GC009052.

Hopkinson, T., Harris, N., Roberts, N. M., Warren, C. J., Hammond, S., Spencer, C. J. & Parrish, R. R. (2020). Evolution of the melt source during protracted crustal anatexis: an example from the Bhutan Himalaya. *Geology* **48**, 87–91. https://doi.org/10.1130/G47078.1.

Horton, F., Lee, J., Hacker, B., Bowman-Kamaha'o, M. & Cosca, M. (2015). Himalayan gneiss dome formation in the middle crust and exhumation by normal faulting: new geochronology of Gianbul dome, northwestern India. *Geological Society of America Bulletin* **127**, 162–180. https://doi.org/10.1130/B31005.1.

Hoskin, P. W. O. & Black, L. P. (2000). Metamorphic zircon formation by solid-state recrystallization of protolith igneous zircon. *Journal of Metamorphic Geology* **18**, 423–439. https://doi.org/10.1046/j.1525-1314.2000.00266.x.

Hoskin, P. W. O. & Schaltegger, U. (2003) The composition of zircon and igneous and metamorphic petrogenesis. In: Hanchar J. M. & Hoskin P. W. O. (eds), *Zircon*. Chantily, Virginia: Mineralogical Society of America, Reviews in Mineralogy and Geochemistry 53, pp. 27–62.

Huang, C. M., Zhao, Z. D., Li, G. M., Zhu, D. C., Liu, D. & Shi, Q. S. (2017). Leucogranites in Lhozag, southern Tibet: implications for the tectonic evolution of the eastern Himalaya. *Lithos* **294-295**, 246–262. https://doi.org/10.1016/j.lithos.2017.09.014.

Imayama, T., Takeshita, T., Yi, K., Cho, D. L., Kitajima, K., Tsutsumi, Y., Kayama, M., Nishido, H., Okumura, T., Yagi, K., Itaya, T. & Sano, Y. (2012). Two-stage partial melting and contrasting cooling history within the Higher Himalayan Crystalline Sequence in the far-eastern Nepal Himalaya. *Lithos* **134-135**, 1–22. https://doi.org/10.1016/j.lithos.2011.12.004.

Inger, S. & Harris, N. (1993). Geochemical constraints on leucogranite magmatism in the Langtang Valley, Nepal Himalaya. *Journal of Petrology* **34**, 345–368. https://doi.org/10.1093/petrology/34.2.345.

Irber, W. (1999). The lanthanide tetrad effect and its correlation with K/Rb, Eu/Eu∗, Sr/Eu, Y/ho, and Zr/Hf of evolving peraluminous granite suites. *Geochimica et Cosmochimica Acta* **63**, 489–508. https://doi.org/10.1016/S0016-7037(99)00027-7.

Jagoutz, O. E. (2010). Construction of the granitoid crust of an island arc. Part II: a quantitative petrogenetic model. *Contributions to Mineralogy and Petrology* **160**, 359–381. https://doi.org/10.1007/s00410-009-0482-6.

Jahn, B. M., Wu, F., Capdevila, R., Martineau, F., Zhao, Z. & Wang, Y. (2001). Highly evolved juvenile granites with tetrad REE patterns: the Woduhe and Baerzhe granites from the Great Xing'an Mountains in NE China. *Lithos* **59**, 171–198. https://doi.org/10.1016/S0024-4937(01)00066-4.

Jamieson, R. A. & Beaumont, C. (2013). On the origin of orogens. *Geological Society of America Bulletin* **125**, 1671–1702. https://doi.org/10.1130/B30855.1.

Jepson, G., Carrapa, B., George, S. W., Reeher, L. J., Kapp, P. A., Davis, G. H., Thomson, S. N., Amadori, C., Clinkscales, C., Jones, S. & Gleadow, A. J. (2022). Where did the Arizonaplano go? Protracted thinning via upper-to lower-crustal processes. *Journal of Geophysical Research: Solid Earth* **127**, e2021JB023850.

Ji, W. Q., Wu, F. Y., Liu, X. C., Liu, Z. C., Zhang, C., Liu, T., Wang, J. G. & Paterson, S. R. (2020). Pervasive Miocene melting of thickened crust from the Lhasa terrane to Himalaya, southern Tibet and its constraint on generation of Himalayan leucogranite. *Geochimica et Cosmochimica Acta* **278**, 137–156. https://doi.org/10.1016/j.gca.2019.07.048.

Ji, M., Gao, X. Y. & Zheng, Y. F. (2022). Geochemical evidence for partial melting of progressively varied crustal sources for leucogranites during the Oligocene–Miocene in the Himalayan orogen. *Chemical Geology* **589**, 120674. https://doi.org/10.1016/j.chemgeo.2021.120674.

Johnson, B. J., Ferguson, C. A., Pearthree, P. A. & Stavast, W. J. (2003). Geologic map of the Samaniego Peak 7½' Quadrangle, Pima County, Arizona. *Arizona Geological Survey Digital Geologic Map* **30**, 21.

Kang, D., Zhang, Z., Palin, R. M., Tian, Z. & Dong, X. (2020). Prolonged partial melting of garnet amphibolite from the eastern Himalayan syntaxis: implications for the tectonic evolution of large hot orogens. *Journal of Geophysical Research: Solid Earth* **125**, e2019JB019119. https://doi.org/10.1029/2019JB019119.

Karlstrom, K. E. & Bowring, S. A. (1993) Proterozoic orogenic history of Arizona. In: Van Schmus W. R. & Bickford M. E. (eds) *Transcontinental Proterozoic Provinces: Precambrian Volume, Decade of North American Geology (DNAG)*. Boulder, Colorado: Geological Society of America, pp. 188–211.

Keith, S. B., Reynolds, S. J., Damon, P. E., Shafiqullah, M., Livingston, D. E. & Pushkar, P. D. (1980) Evidence for multiple intrusion and deformation within the Santa Catalina-Rincon-Tortolita crystalline complex, southeastern Arizona. In: Crittenden M., Coney P. & Davis G. (eds) *Cordilleran Metamorphic Core Complexes*. Geological Society of America Memoir 153, pp. 217–267.

Kelly, N. M. & Harley, S. L. (2005). An integrated microtextural and chemical approach to zircon geochronology: refining the Archaean history of the Napier Complex, east Antarctica. *Contributions to Mineralogy and Petrology* **149**, 57–84. https://doi.org/10.1007/s00410-004-0635-6.

Kelsey, D. E. & Powell, R. (2011). Progress in linking accessory mineral growth and breakdown to major mineral evolution in metamorphic rocks: a thermodynamic approach in the Na2O-CaO-K2O-FeO-MgO-Al2O3-SiO2-H2O-TiO2-ZrO2 system. *Journal of Metamorphic Geology* **29**, 151–166. https://doi.org/10.1111/j.1525-1314.2010.00910.x.

Kerrich, R. & Rehrig, W. (1987). Fluid motion associated with tertiary mylonitization and detachment faulting: $^{18}O/^{16}O$ evidence from the Picacho metamorphic core complex, Arizona. *Geology* **15**, 58–62. https://doi.org/10.1130/0091-7613(1987)15<58:FMAWTM>2.0.CO;2.

King, J., Harris, N., Argles, T., Parrish, R. & Zhang, H. (2011). Contribution of crustal anatexis to the tectonic evolution of Indian crust beneath southern Tibet. *Geological Society of America Bulletin* **123**, 218–239. https://doi.org/10.1130/B30085.1.

Kirkland, C. L., Smithies, R. H., Taylor, R. J. M., Evans, N. & McDonald, B. (2015). Zircon Th/U ratios in magmatic environs. *Lithos* **212-215**, 397–414. https://doi.org/10.1016/j.lithos.2014.11.021.

Kirkland, C. L., Slagstad, T. & Johnson, T. E. (2018). Zircon as a metamorphic timekeeper: a case study from the Caledonides of central Norway. *Gondwana Research* **61**, 63–72. https://doi.org/10.1016/j.gr.2018.05.005.

Klemperer, S. L. (2006). Crustal flow in Tibet: geophysical evidence for the physical state of Tibetan lithosphere, and inferred patterns of active flow. *Geological Society, London, Special Publication* **268**, 39–70. https://doi.org/10.1144/GSL.SP.2006.268.01.03.

Kohn, M. J. (2014). Himalayan metamorphism and its tectonic implications. *Annual Review of Earth and Planetary Sciences* **42**, 381–419. https://doi.org/10.1146/annurev-earth-060313-055005.

Kohn, M. J. (2017). Titanite petrochronology. *Reviews in Mineralogy and Geochemistry* **83**, 419–441. https://doi.org/10.2138/rmg.2017.83.13.

Kohn, M. J. & Kelly, N. M. (2018) Petrology and geochronology of metamorphic zircon. In: Moser D. E., Corfu F., Darling J. R., Reddy S. M. & Tait K. (eds) *Microstructural Geochronology: Planetary Records Down to Atom Scale*. American Geophysical Union Monograph 232, pp. 35–61.

Kohn, M. J., Corrie, S. L. & Markley, C. (2015). The fall and rise of metamorphic zircon. *American Mineralogist* **100**, 897–908. https://doi.org/10.2138/am-2015-5064.

Krogh, T. E. & Davis, G. L. (1975). Alteration in zircons and differential dissolution of altered and metamict zircon. *Carnegie Institution of Washington Year Book* **74**, 619–623.

Kumar, P., Yuan, X., Kind, R. & Mechie, J. (2012). The lithosphere-asthenosphere boundary observed with US Array receiver functions. *Solid Earth* **3**, 149–159. https://doi.org/10.5194/se-3-149-2012.

Langille, J. M., Jessup, M. J., Cottle, J. M., Lederer, G. & Ahmad, T. (2012). Timing of metamorphism, melting and exhumation of the Leo Pargil dome, northwest India. *Journal of Metamorphic Geology* **30**, 769–791. https://doi.org/10.1111/j.1525-1314.2012.00998.x.

Laurent, O., Couzinié, S., Zeh, A., Vanderhaeghe, O., Moyen, J. F., Villaros, A., Gardien, V. & Chelle-Michou, C. (2017). Protracted, coeval crust and mantle melting during Variscan late-orogenic evolution: U–Pb dating in the eastern French Massif Central. *International Journal of Earth Sciences* **106**, 421–451. https://doi.org/10.1007/s00531-016-1434-9.

Le Fort, P., Cuney, M., Deniel, C., France-Lanord, C., Sheppard, S. M. F., Upreti, B. N. & Vidal, P. (1987). Crustal generation of the Himalayan leucogranites. *Tectonophysics* **134**, 39–57. https://doi.org/10.1016/0040-1951(87)90248-4.

Lederer, G. W., Cottle, J. M., Jessup, M. J., Langille, J. M. & Ahmad, T. (2013). Timescales of partial melting in the Himalayan middle crust: insight from the Leo Pargil dome, northwest India. *Contributions to Mineralogy and Petrology* **166**, 1415–1441. https://doi.org/10.1007/s00410-013-0935-9.

Lin, C., Zhang, J., Wang, X., Putthapiban, P., Zhang, B. & Huang, T. (2020). Oligocene initiation of the south Tibetan detachment system: constraints from syn-tectonic leucogranites in the Kampa dome, northern Himalaya. *Lithos* **354-355**, 105332. https://doi.org/10.1016/j.lithos.2019.105332.

Linnen, R. L. & Keppler, H. (2002). Melt composition control of Zr/Hf fractionation in magmatic processes. *Geochimica et Cosmochimica Acta* **66**, 3293–3301. https://doi.org/10.1016/S0016-7037(02)00924-9.

Liu, S. & Currie, C. A. (2016). Farallon plate dynamics prior to the Laramide orogeny: numerical models of flat subduction. *Tectonophysics* **666**, 33–47. https://doi.org/10.1016/j.tecto.2015.10.010.

Liu, Z. C., Wu, F. Y., Ji, W. Q., Wang, J. G. & Liu, C. Z. (2014). Petrogenesis of the Ramba leucogranite in the Tethyan Himalaya and constraints on the channel flow model. *Lithos* **208-209**, 118–136. https://doi.org/10.1016/j.lithos.2014.08.022.

Liu, Z. C., Wu, F. Y., Ding, L., Liu, X. C., Wang, J. G. & Ji, W. Q. (2016). Highly fractionated Late Eocene (~35 Ma) leucogranite in the Xiaru Dome, Tethyan Himalaya, South Tibet. *Lithos* **240-243**, 337–354. https://doi.org/10.1016/j.lithos.2015.11.026.

Liu, Z. C., Wu, F. Y., Liu, X. C., Wang, J. G., Yin, R., Qiu, Z. L., Ji, W. Q. & Yang, L. (2019). Mineralogical evidence for fractionation processes in the Himalayan leucogranites of the Ramba Dome, southern Tibet. *Lithos* **340-341**, 71–86. https://doi.org/10.1016/j.lithos.2019.05.004.

Loader, M. A., Nathwani, C. L., Wilkinson, J. J. & Armstrong, R. N. (2022). Controls on the magnitude of Ce anomalies in zircon. *Geochimica et Cosmochimica Acta* **328**, 242–257. https://doi.org/10.1016/j.gca.2022.03.024.

Loucks, R. R., Fiorentini, M. L. & Henríquez, G. J. (2020). New magmatic oxybarometer using trace elements in zircon. *Journal of Petrology* **61**, egaa034. https://doi.org/10.1093/petrology/egaa034.

Marsh, J. H. & Stockli, D. F. (2015). Zircon U–Pb and trace element zoning characteristics in an anatectic granulite domain: insights from LASS-ICP-MS depth profiling. *Lithos* **239**, 170–185. https://doi.org/10.1016/j.lithos.2015.10.017.

Matthews, N. E., Vazquez, J. A. & Calvert, A. T. (2015). Age of the Lava Creek supereruption and magma chamber assembly at

Yellowstone based on $^{40}Ar/^{39}Ar$ and U-Pb dating of sanidine and zircon crystals. *Geochemistry, Geophysics, Geosystems* **16**, 2508–2528. https://doi.org/10.1002/2015GC005881.

Mattinson, J. M. (2005). Zircon U-Pb chemical abrasion ("CATIMS") method: combined annealing and multistep partial dissolution analysis for improved precision and accuracy of zircon ages. *Chemical Geology* **220**, 47–66. https://doi.org/10.1016/j.chemgeo.2005.03.011.

McDonough, W. F. & Sun, S. S. (1995). The composition of the Earth. *Chemical Geology* **120**, 223–253. https://doi.org/10.1016/0009-2541(94)00140-4.

McLennan, S. M. (1994). Rare earth element geochemistry and the "tetrad" effect. *Geochimica et Cosmochimica Acta* **58**, 2025–2033. https://doi.org/10.1016/0016-7037(94)90282-8.

Meijer, A. (2014). The Pinal Schist of southern Arizona: a Paleoproterozoic forearc complex with evidence of spreading ridge–trench interaction at ca. 1.65 Ga and a Proterozoic arc obduction event. *Geological Society of America Bulletin* **126**, 1145–1163. https://doi.org/10.1130/B31002.1.

Miller, C. F. & Mittlefehldt, D. W. (1982). Depletion of light rare-earth elements in felsic magmas. *Geology* **10**, 129–133. https://doi.org/10.1130/0091-7613(1982)10<129:DOLREI>2.0.CO;2.

Molnar, P. & England, P. (1990). Temperatures, heat flux, and frictional stress near major thrust faults. *Journal of Geophysical Research: Solid Earth* **95**, 4833–4856. https://doi.org/10.1029/JB095iB04p04833.

Molnar, P., England, P. & Martinod, J. (1993). Mantle dynamics, uplift of the Tibetan Plateau, and the Indian monsoon. *Reviews of Geophysics* **31**, 357–396. https://doi.org/10.1029/93RG02030.

Nabelek, P. I. (2019). Petrogenesis of leucogranites in collisional orogens. *Geological Society, London, Special Publication* **491**, 179–207.

Nabelek, P. I. & Liu, M. (1999). Leucogranites in the Black Hills of South Dakota: the consequence of shear heating during continental collision. *Geology* **27**, 523–526. https://doi.org/10.1130/0091-7613(1999)027<0523:LITBHO>2.3.CO;2.

Nasdala, L., Hanchar, J. M., Rhede, D., Kennedy, A. K. & Váczi, T. (2010). Retention of uranium in complexly altered zircon: an example from Bancroft, Ontario. *Chemical Geology* **269**, 290–300. https://doi.org/10.1016/j.chemgeo.2009.10.004.

Nelson, K. D., Zhao, W., Brown, L. D., Kuo, J., Che, J., Liu, X., Klemperer, S. L., Makovsky, Y., Meissner, R. J. J. M., Mechie, J., Kind, R., Wenzel, F., Ni, J., Nabelek, J., Leshou, C., Tan, H., Wei, W., Jones, A. G., Booker, J., Unsworth, M., Kidd, W. S. F., Hauck, M., Alsdorf, D., Ross, A., Cogan, M., Wu, C., Sandvol, E. & Edwards, M. (1996). Partially molten middle crust beneath southern Tibet: synthesis of project INDEPTH results. *Science* **274**, 1684–1688. https://doi.org/10.1126/science.274.5293.1684.

Park, C., Song, Y., Chung, D., Kang, I. M., Khulganakhuu, C. & Yi, K. (2016). Recrystallization and hydrothermal growth of high U–Th zircon in the Weondong deposit, Korea: record of post-magmatic alteration. *Lithos* **260**, 268–285. https://doi.org/10.1016/j.lithos.2016.05.026.

Patiño-Douce, A. E. (1999). What do experiments tell us about the relative contributions of crust and mantle to the origin of granitic magmas? *Geological Society, London, Special Publication* **168**, 55–75. https://doi.org/10.1144/GSL.SP.1999.168.01.05.

Patiño-Douce, A. E. & Harris, N. (1998). Experimental constraints on Himalayan anatexis. *Journal of Petrology* **39**, 689–710. https://doi.org/10.1093/petroj/39.4.689.

Patiño-Douce, P., Humphreys, E. D. & Johnston, A. D. (1990). Anatexis and metamorphism in tectonically thickened continental crust exemplified by the Sevier hinterland, western North America. *Earth and Planetary Science Letters* **97**, 290–315. https://doi.org/10.1016/0012-821X(90)90048-3.

Pedrosa-Soares, A. C., Noce, C. M., Wiedemann, C. M. & Pinto, C. P. (2001). The Araçuaı-West-Congo Orogen in Brazil: an overview of a confined orogen formed during Gondwanaland assembly. *Precambrian Research* **110**, 307–323. https://doi.org/10.1016/S0301-9268(01)00174-7.

Pidgeon, R. T., Nemchin, A. A. & Hitchen, G. J. (1998). Internal structures of zircons from Archaean granites from the Darling Range batholith: implications for zircon stability and the interpretation of zircon U-Pb ages. *Contributions to Mineralogy and Petrology* **132**, 288–299. https://doi.org/10.1007/s004100050422.

Platt, J. P. (2015). Influence of shear heating on microstructurally defined plate boundary shear zones. *Journal of Structural Geology* **79**, 80–89. https://doi.org/10.1016/j.jsg.2015.07.009.

Quintero, R. R., Kitajima, K., Lackey, J. S., Kozdon, R., Strickland, A. & Valley, J. W. (2021). Oxygen isotope ratios in zircon and garnet: a record of assimilation and fractional crystallization in the Dinkey Dome peraluminous granite, Sierra Nevada, California. *American Mineralogist* **106**, 715–729. https://doi.org/10.2138/am-2021-7472.

Rubatto, D. (2017). Zircon: the metamorphic mineral. *Reviews in Mineralogy and Geochemistry* **83**, 261–295. https://doi.org/10.2138/rmg.2017.83.9.

Rubatto, D. & Gebauer, D. (2000) Use of cathodoluminescence for U-Pb zircon dating by ion microprobe: some examples from the Western Alps. In: Pagel M., Barbin V., Blanc P. & Ohnenstetter D. (eds) *Cathodoluminescence in Geosciences*. Berlin: Springer Verlag, pp. 373–400.

Rubatto, D., Hermann, J., Berger, A. & Engi, M. (2009). Protracted fluid-induced melting during Barrovian metamorphism in the Central Alps. *Contributions to Mineralogy and Petrology* **158**, 703–722. https://doi.org/10.1007/s00410-009-0406-5.

Rubatto, D., Chakraborty, S. & Dasgupta, S. (2013). Timescales of crustal melting in the higher Himalayan crystallines (Sikkim, Eastern Himalaya) inferred from trace element-constrained monazite and zircon chronology. *Contributions to Mineralogy and Petrology* **165**, 349–372. https://doi.org/10.1007/s00410-012-0812-y.

Sano, Y., Terada, K. & Fukuoka, T. (2002). High mass resolution ion microprobe analysis of rare earth elements in silicate glass, apatite and zircon: lack of matrix dependency. *Chemical Geology* **184**, 217–230. https://doi.org/10.1016/S0009-2541(01)00366-7.

Scaillet, B., France-Lanord, C. & Le Fort, P. (1990). Badrinath-Gangotri plutons (Garhwal, India): petrological and geochemical evidence for fractionation processes in a high Himalayan leucogranite. *Journal of Volcanology and Geothermal Research* **44**, 163–188. https://doi.org/10.1016/0377-0273(90)90017-A.

Scaillet, B., Pêcher, A., Rochette, P. & Champenois, M. (1995). The Gangotri granite (Garhwal Himalaya): laccolithic emplacement in an extending collisional belt. *Journal of Geophysical Research: Solid Earth* **100**, 585–607. https://doi.org/10.1029/94JB01664.

Schaltegger, U., Fanning, C. M., Günther, D., Maurin, J. C., Schulmann, K. & Gebauer, D. (1999). Growth, annealing and recrystallization of zircon and preservation of monazite in high-grade metamorphism: conventional and in-situ U-Pb isotope, cathodoluminescence and microchemical evidence. *Contributions to Mineralogy and Petrology* **134**, 186–201. https://doi.org/10.1007/s004100050478.

Schaltegger, U., Gebauer, D. & von Quadt, A. (2002). The mafic–ultramafic rock association of Loderio–Biasca (lower Pennine nappes, Ticino, Switzerland): Cambrian oceanic magmatism and its bearing on early Paleozoic paleogeography. *Chemical Geology* **186**, 265–279. https://doi.org/10.1016/S0009-2541(02)00005-0.

Schiller, D. & Finger, F. (2019). Application of Ti-in-zircon thermometry to granite studies: problems and possible solutions. *Contributions to Mineralogy and Petrology* **174**, 1–16. https://doi.org/10.1007/s00410-019-1585-3.

Schilling, F. R., Trumbull, R. B., Brasse, H., Haberland, C., Asch, G., Bruhn, D., Mai, K., Haak, V., Giese, P., Muñoz, M., Ramelow, J., Rietbrock, A., Ricaldi, E. & Vietor, T. (2006) Partial melting in the Central Andean crust: a review of geophysical, petrophysical, and petrologic evidence. In: Oncken O., Chong G., Franz G., Giese P., Gotze H. J., Ramos V., Strecker M. & Wigger P. (eds) *The Andes: Active Subduction Orogeny*. Berlin, Germany: Springer, pp. 459–474.

Schwindinger, M., Weinberg, R. F. & Clos, F. (2019). Wet or dry? The difficulty of identifying the presence of water during crustal melting. *Journal of Metamorphic Geology* **37**, 339–358. https://doi.org/10.1111/jmg.12465.

Scoggin, S. H., Chapman, J. B., Shields, J. E., Trzinski, A. E. & Ducea, M. N. (2021). Early Paleogene Magmatism in the Pinaleño Mountains, Arizona: evidence for crustal melting of diverse basement assemblages during the Laramide orogeny. *Journal of Petrology* **62**, egab095. https://doi.org/10.1093/petrology/egab095.

Seedorff, E., Barton, M. D., Gehrels, G. E., Valencia, V. A., Johnson, D. A., Maher, D. J., Stavast, W. J. & Marsh, T. M. (2019) Temporal evolution of the Laramide arc: U-Pb geochronology of plutons associated with porphyry copper mineralization in east-central Arizona. In: Pearthree P. A. (ed) *Geologic Excursions in Southwestern North America. Geological Society of America Field Guide* 55, Boulder, Colorado: Geological Society of America, pp. 369–400.

Soman, A., Geisler, T., Tomaschek, F., Grange, M. & Berndt, J. (2010). Alteration of crystalline zircon solid solutions: a case study on zircon from an alkaline pegmatite from Zomba–Malosa, Malawi. *Contributions to Mineralogy and Petrology* **160**, 909–930. https://doi.org/10.1007/s00410-010-0514-2.

Stepanov, A. S., Hermann, J., Rubatto, D. & Rapp, R. P. (2012). Experimental study of monazite/melt partitioning with implications for the REE, Th and U geochemistry of crustal rocks. *Chemical Geology* **300-301**, 200–220. https://doi.org/10.1016/j.chemgeo.2012.01.007.

Tichomirowa, M., Whitehouse, M. J. & Nasdala, L. (2005). Resorption, growth, solid state recrystallisation, and annealing of granulite facies zircon—a case study from the Central Erzgebirge, bohemian massif. *Lithos* **82**, 25–50. https://doi.org/10.1016/j.lithos.2004.12.005.

Tomaschek, F., Kennedy, A. K., Villa, I. M., Lagos, M. & Ballhaus, C. (2003). Zircons from Syros, Cyclades, Greece—recrystallization and mobilization of zircon during high-pressure metamorphism. *Journal of Petrology* **44**, 1977–2002. https://doi.org/10.1093/petrology/egg067.

Tosdal, R. M. & Wooden, J. L. (2015) Construction of the Jurassic magmatic arc, southeast California and southwest Arizona. In: Anderson T., Didenko A., Johnson C., Khanchuk A. & McDonald J. (eds) *Late Jurassic Margin of Laurasia – A Record of Faulting Accommodating Plate Rotation*. Geological Society of America *Special Paper* 513, p. 189–221.

Troch, J., Ellis, B. S., Schmitt, A. K., Bouvier, A. S. & Bachmann, O. (2018). The dark side of zircon: textural, age, oxygen isotopic and trace element evidence of fluid saturation in the subvolcanic reservoir of the Island Park-Mount Jackson Rhyolite, Yellowstone (USA). *Contributions to Mineralogy and Petrology* **173**, 1–17. https://doi.org/10.1007/s00410-018-1481-2.

Turi, B. & Taylor, H. P. (1971). O^{18}/O^{16} ratios of the Johnny Lyon granodiorite and Texas Canyon quartz monzonite plutons, Arizona, and their contact aureoles. *Contributions to Mineralogy and Petrology* **32**, 138–146. https://doi.org/10.1007/BF00383056.

Unsworth, M. J., Jones, A. G., Wei, W., Marquis, G., Gokarn, S. G., Spratt, J. E., Bedrosian, P., Booker, J., Leshou, C., Clarke, G., Shenghui, L., Chanhong, L., Ming, D., Sheng, J., Solon, K., Handong, T., Ledo, J., Roberts, B. & INDEPTH-MT team (2005). Crustal rheology of the Himalaya and Southern Tibet inferred from magnetotelluric data. *Nature* **438**, 78–81. https://doi.org/10.1038/nature04154.

Van Lichtervelde, M., Melcher, F. & Wirth, R. (2009). Magmatic vs. hydrothermal origins for zircon associated with tantalum mineralization in the Tanco pegmatite, Manitoba, Canada. *American Mineralogist* **94**, 439–450. https://doi.org/10.2138/am.2009.2952.

Vanderhaeghe, O., Medvedev, S., Fullsack, P., Beaumont, C. & Jamieson, R. A. (2003). Evolution of orogenic wedges and continental plateaux: insights from crustal thermal–mechanical models overlying subducting mantle lithosphere. *Geophysical Journal International* **153**, 27–51. https://doi.org/10.1046/j.1365-246X.2003.01861.x.

Vavra, G., Gebauer, D., Schmid, R. & Compston, W. (1996). Multiple zircon growth and recrystallization during polyphase Late Carboniferous to Triassic metamorphism in granulites of the Ivrea Zone (Southern Alps): an ion microprobe (SHRIMP) study. *Contributions to Mineralogy and Petrology* **122**, 337–358. https://doi.org/10.1007/s004100050132.

Vavra, G., Schmid, R. & Gebauer, D. (1999). Internal morphology, habit and U-Th-Pb microanalysis of amphibolite-to-granulite facies zircons: geochronology of the Ivrea Zone (Southern Alps). *Contributions to Mineralogy and Petrology* **134**, 380–404. https://doi.org/10.1007/s004100050492.

Villaseca, C., Barbero, L. & Rogers, G. (1998). Crustal origin of Hercynian peraluminous granitic batholiths of Central Spain: petrological, geochemical and isotopic (Sr, Nd) constraints. *Lithos* **43**, 55–79. https://doi.org/10.1016/S0024-4937(98)00002-4.

Viskupic, K., Hodges, K. V. & Bowring, S. A. (2005). Timescales of melt generation and the thermal evolution of the Himalayan metamorphic core, Everest region, eastern Nepal. *Contributions to Mineralogy and Petrology* **149**, 1–21. https://doi.org/10.1007/s00410-004-0628-5.

Visonà, D. & Lombardo, B. (2002). Two-mica and tourmaline leucogranites from the Everest–Makalu region (Nepal–Tibet). Himalayan leucogranite genesis by isobaric heating? *Lithos* **62**, 125–150. https://doi.org/10.1016/S0024-4937(02)00112-3.

Visonà, D., Carosi, R., Montomoli, C., Tiepolo, M. & Peruzzo, L. (2012). Miocene andalusite leucogranite in central-east Himalaya (Everest–Masang Kang area): low-pressure melting during heating. *Lithos* **144-145**, 194–208. https://doi.org/10.1016/j.lithos.2012.04.012.

Vonlanthen, P., Fitz Gerald, J. D., Rubatto, D. & Hermann, J. (2012). Recrystallization rims in zircon (Valle d'Arbedo, Switzerland): an integrated cathodoluminescence, LA-ICP-MS, SHRIMP, and TEM study. *American Mineralogist* **97**, 369–377. https://doi.org/10.2138/am.2012.3854.

Wang, Z. Z., Liu, S. A., Liu, Z. C., Zheng, Y. C. & Wu, F. Y. (2020). Extreme Mg and Zn isotope fractionation recorded in the Himalayan leucogranites. *Geochimica et Cosmochimica Acta* **278**, 305–321. https://doi.org/10.1016/j.gca.2019.09.026.

Ward, K. M., Delph , J. R., Zandt, G., Beck, S. L. & Ducea, M. N. (2017). Magmatic evolution of a Cordilleran flare-up and its role in the creation of silicic crust. *Scientific Reports* **7**, 1–8. https://doi.org/10.1038/s41598-017-09015-5.

Weinberg, R. F. (2016). Himalayan leucogranites and migmatites: nature, timing and duration of anatexis. *Journal of Metamorphic Geology* **34**, 821–843. https://doi.org/10.1111/jmg.12204.

Weinberg, R. F. & Hasalová, P. (2015). Water-fluxed melting of the continental crust: a review. *Lithos* **212-215**, 158–188. https://doi.org/10.1016/j.lithos.2014.08.021.

Wells, M. L. & Hoisch, T. D. (2008). The role of mantle delamination in widespread Late Cretaceous extension and magmatism in the Cordilleran orogen, western United States. *Geological Society of America Bulletin* **120**, 515–530. https://doi.org/10.1130/B26006.1.

Whitney, D. L., Teyssier, C. & Fayon, A. K. (2004). Isothermal decompression, partial melting and exhumation of deep continental crust. *Geological Society, London, Special Publication* **227**, 313–326. https://doi.org/10.1144/GSL.SP.2004.227.01.16.

Wong, M. S., Singleton, J. S., Seymour, N. M., Gans, P. B. & Wrobel, A. J. (2023). Late Cretaceous-early Paleogene extensional ancestry of the Harcuvar and Buckskin-Rawhide metamorphic core complexes, Western Arizona. *Tectonics* **42**, e2022TC007656. https://doi.org/10.1029/2022TC007656.

Wright, J. E. & Haxel, G. (1982). A garnet-two-mica granite, Coyote Mountains, southern Arizona: geologic setting, uranium-lead isotopic systematics of zircon, and nature of the granite source region. *Geological Society of America Bulletin* **93**, 1176–1188. https://doi.org/10.1130/0016-7606(1982)93<1176:AGGCMS>2.0.CO;2.

Wu, F. Y., Liu, X. C., Liu, Z. C., Wang, R. C., Xie, L., Wang, J. M., Ji, W. Q., Yang, L., Liu, C., Khanal, G. P. & He, S. X. (2020). Highly fractionated Himalayan leucogranites and associated rare-metal mineralization. *Lithos* **352-353**, 105319. https://doi.org/10.1016/j.lithos.2019.105319.

Xie, J., Qiu, H., Bai, X., Zhang, W., Wang, Q. & Xia, X. (2018). Geochronological and geochemical constraints on the Cuonadong leucogranite, eastern Himalaya. *Acta Geochimica* **37**, 347–359. https://doi.org/10.1007/s11631-018-0273-8.

Yakymchuk, C. (2017). Behaviour of apatite during partial melting of metapelites and consequences for prograde suprasolidus monazite growth. *Lithos* **274**, 412–426. https://doi.org/10.1016/j.lithos.2017.01.009.

Yakymchuk, C. (2023). Prograde zircon growth in migmatites. *Journal of Metamorphic Geology* **41**, 719–743. https://doi.org/10.1111/jmg.12715.

Yakymchuk, C. & Brown, M. (2019). Divergent behaviour of Th and U during anatexis: implications for the thermal evolution of orogenic crust. *Journal of Metamorphic Geology* **37**, 899–916. https://doi.org/10.1111/jmg.12469.

Yakymchuk, C., Clark, C. & White, R. W. (2017). Phase relations, reaction sequences and petrochronology. *Reviews in Mineralogy and Geochemistry* **83**, 13–53. https://doi.org/10.2138/rmg.2017.83.2.

Yakymchuk, C., Kirkland, C. L. & Clark, C. (2018). Th/U ratios in metamorphic zircon. *Journal of Metamorphic Geology* **36**, 715–737. https://doi.org/10.1111/jmg.12307.

Yang, L., Liu, X. C., Wang, J. M. & Wu, F. Y. (2019). Is Himalayan leucogranite a product by in situ partial melting of the Greater Himalayan Crystalline? A comparative study of leucosome and leucogranite from Nyalam, southern Tibet. *Lithos* **342-343**, 542–556. https://doi.org/10.1016/j.lithos.2019.06.007.

Yang, L., Miller, C. F. & Wu, F. Y. (2022). Estimating crystallization pressure of peraluminous melts: an experimentally based empirical approach. *Contributions to Mineralogy and Petrology* **177**, 78. https://doi.org/10.1007/s00410-022-01945-2.

Yu, S., Li, S., Zhang, J., Peng, Y., Somerville, I., Liu, Y., Wang, Z., Li, Z., Yao, Y. & Li, Y. (2019). Multistage anatexis during tectonic evolution from oceanic subduction to continental collision: a review of the North Qaidam UHP Belt, NW China. *Earth-Science Reviews* **191**, 190–211. https://doi.org/10.1016/j.earscirev.2019.02.016.

Zamyatin, D. A., Shchapova, Y. V., Votyakov, S. L., Nasdala, L. & Lenz, C. (2017). Alteration and chemical U-Th-total Pb dating of heterogeneous high-uranium zircon from a pegmatite from the Aduiskii Massif, Middle Urals, Russia. *Mineralogy and Petrology* **111**, 475–497. https://doi.org/10.1007/s00710-017-0513-3.

Zeng, L., Gao, L. E., Xie, K. & Liu-Zeng, J. (2011). Mid-Eocene high Sr/Y granites in the Northern Himalayan Gneiss Domes: melting thickened lower continental crust. *Earth and Planetary Science Letters* **303**, 251–266. https://doi.org/10.1016/j.epsl.2011.01.005.

Zeng, L., Gao, L. E., Tang, S., Hou, K., Guo, C. & Hu, G. (2015) Eocene magmatism in the Tethyan Himalaya, southern Tibet. In: Mukherjee S., Carosi R., van der Beek P. A., Mukherjee B. K. & Robinson D. M. (eds) *Tectonics of the Himalaya*. London: Geological Society, Special Publication 412, pp. 287–316.

Zhang, H., Harris, N., Parrish, R., Kelley, S., Zhang, L., Rogers, N., Argles, T. & King, J. (2004). Causes and consequences of protracted melting of the mid-crust exposed in the north Himalayan antiform. *Earth and Planetary Science Letters* **228**, 195–212. https://doi.org/10.1016/j.epsl.2004.09.031.

Zhang, Z., Xiang, H., Dong, X., Li, W., Ding, H., Gou, Z. & Tian, Z. (2017). Oligocene HP metamorphism and anatexis of the Higher Himalayan Crystalline Sequence in Yadong region, east-central Himalaya. *Gondwana Research* **41**, 173–187. https://doi.org/10.1016/j.gr.2015.03.002.